ATLAS CONF Note

ATLAS-CONF-2020-055

5th November 2020

Constraints on Higgs boson properties using $WW^*(\to e\nu\mu\nu)jj$ production in 36.1 fb^{-1} of $\sqrt{s} = 13$ TeV pp collisions with the ATLAS detector

The ATLAS Collaboration

This note presents the results of two studies of Higgs boson properties using the $WW^*(\to e\nu\mu\nu)jj$ final state, based on a dataset corresponding to 36.1 fb^{-1} of $\sqrt{s} = 13$ TeV proton-proton collisions recorded by the ATLAS experiment at the Large Hadron Collider. The first study targets Higgs boson production via gluon fusion and constrains the CP properties of the effective Higgs-gluon vertex for the first time in the $e\nu\mu\nu jj$ final state. Using both angular distributions and the overall rate, the ratio of the CP-odd to CP-even coupling strength scale factors of the effective Higgs-gluon vertex is constrained to $\kappa_{Agg}/\kappa_{Hgg} = 0.0 \pm 0.4(\text{stat.}) \pm 0.3(\text{syst.})$. The second study investigates vector boson fusion to individually access the Higgs boson couplings to longitudinally and transversely polarised W and Z bosons in both the production and the decay of the Higgs boson; these polarisations have not been previously constrained in this process. The polarisation coupling-strength scale factors, defined as the ratios of the measured polarisation-dependent coupling strengths to those predicted by the Standard Model, are constrained using shape and rate information to the values $a_{\text{L}} = 0.91^{+0.10}_{-0.18}(\text{stat.})^{+0.09}_{-0.18}(\text{syst.})$ and $a_{\text{T}} = 1.16 \pm 0.4(\text{stat.})^{+0.4}_{-0.3}(\text{syst.})$ These coupling strengths are translated into pseudo-observables, resulting in $\kappa_{VV} = 0.90^{+0.10}_{-0.18}(\text{stat.})^{+0.09}_{-0.16}(\text{syst.})$ and $\epsilon_{VV} = 0.13^{+0.28}_{-0.20}(\text{stat.})^{+0.08}_{-0.10}(\text{syst.})$. All results are consistent with the SM predictions.

1 Introduction

The Higgs boson discovery at the Large Hadron Collider (LHC) was a great success of the ATLAS and CMS Collaborations [1, 2]. Following the discovery, multiple studies have been performed to establish whether it is a Standard Model (SM) particle or rather a particle of a, hitherto unobserved, beyond the Standard Model (BSM) sector. The mass of this particle has been measured by the ATLAS and CMS collaborations to be $m_H = 125.09 \pm 0.21(\text{stat.}) \pm 0.11(\text{syst.})$ GeV [3], and there are strong hints for the spin and parity states to be $J^P = 0^+$ [4–6]. By probing the final state particles in $H \rightarrow WW^*$, $H \rightarrow ZZ^*$ and $H \rightarrow \gamma\gamma$ decays, a pure CP odd Higgs boson has been excluded at more than 99.9% confidence level. In addition, a potential CP odd contribution to the HWW and HZZ coupling has been significantly constrained [7–9]. Recently the studies of the CP properties of the top Yukawa coupling using Htt events have been published [10, 11]. However, the CP nature of the effective coupling between the Higgs boson and gluons, ggH, in the gluon-fusion-induced production mode [12] has not been studied yet in a dedicated analysis. The gluon fusion process probes a different kinematic regime than Htt production, and the properties of the effective ggH vertex itself may differ from SM predictions if there is a loop contribution from previously unobserved particles. Therefore, the analysis presents a novel and complementary approach to those used in existing studies of the CP properties of the Higgs boson.

The VBF Higgs boson production process was measured by ATLAS and CMS in numerous channels [7, 13–17]. While measurements of $\sigma_{\text{VBF}} \cdot \mathcal{B}_{H \rightarrow WW}$ are consistent with the SM, individual polarisation-dependent Higgs couplings to the electroweak massive bosons have so far not been studied. Longitudinally polarised electroweak bosons emerge from massless degrees of freedom of the Higgs boson and are therefore closely related to the mechanism of EWSB. The strength of the Higgs coupling to longitudinally polarised W bosons ensures the unitarity of the SM. However, if the Higgs field is not a fundamental scalar particle but an effective field arising from new dynamics, the coupling may deviate from its SM value. For example, Higgs compositeness models [18, 19] predict more degrees of freedom, allowing the Higgs couplings to electroweak bosons to deviate from their SM values.

This note presents results of two analyses studying the properties of the Higgs boson using its decay to $WW^* \rightarrow e\nu\mu\nu$ and its production in association with two jets. The first analysis targets gluon fusion (ggF) Higgs boson production and aims to constrain CP properties of the top Yukawa coupling, effects from new particles in the gluon-fusion loop, or a combination of both effects. The second analysis constrains Higgs boson couplings to longitudinally and transversely polarised W and Z bosons in the vector boson fusion (VBF) production mode, assuming a CP-even Higgs boson. Both studies are based on proton–proton collision data corresponding to an integrated luminosity of 36.1 fb^{-1} collected with the ATLAS detector at $\sqrt{s} = 13$ TeV in the years 2015 and 2016. Exemplary leading order diagrams for the ggF + 2 jets and VBF production modes are depicted in Figure 1 (a)–(c) and (d), respectively.

Both analyses use the shape of the signed azimuthal angle[1] difference $\Delta\Phi_{jj}$ between the two leading jets in the selected H + 2 jets candidate events in order to find deviations from the SM expectations. The angle is defined as $\Delta\Phi_{jj} = \phi_{j_1} - \phi_{j_2}$ if $\eta_{j_1} > \eta_{j_2}$, and $\Delta\Phi_{jj} = \phi_{j_2} - \phi_{j_1}$ otherwise, where j_1 is the highest p_{T} and j_2 the next-highest p_{T} jet in the event. $\Delta\Phi_{jj}$ is probed in various disjoint phase space regions, optimised for each analysis specifically.

---

[1] ATLAS uses a right-handed coordinate system with its origin at the nominal interaction point (IP) in the centre of the detector and the z-axis along the beam pipe. The x-axis points from the IP to the centre of the LHC ring, and the y-axis points upwards. Cylindrical coordinates (r, ϕ) are used in the transverse plane, ϕ being the azimuthal angle around the beam pipe. The pseudorapidity is defined in terms of the polar angle θ as $\eta = -\ln\tan(\theta/2)$. Angular distance is measured in units of $\Delta R \equiv \sqrt{(\Delta\eta)^2 + (\Delta\phi)^2}$.
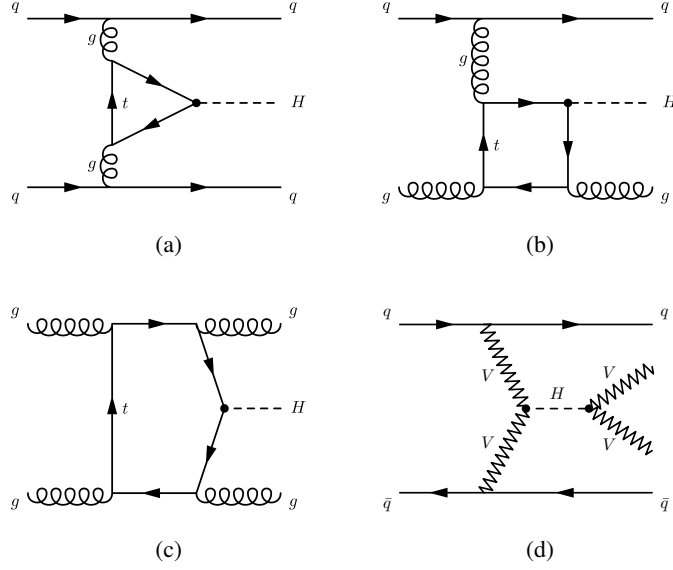
Figure 1: Examples of Feynman diagrams contributing to the production of a Higgs boson in association with two jets via the fusion of two gluons or two vector bosons at LO in QCD. The presented diagrams show examples for (a) the subprocesses $qq \rightarrow Hqq$, (b) $qg \rightarrow Hqg$ and (c) $gg \rightarrow Hgg$, as well as (d) the vector boson fusion process and the subsequent decay of the Higgs boson to two vector bosons.

The structure of this note is as follows. Section 2 gives a short summary of the theoretical frameworks used to study the CP properties of the Higgs-boson coupling to top quarks and gluons, as well as its coupling to polarised electroweak bosons. The ATLAS detector and the Monte Carlo and data samples used in these studies are discussed in Section 3 and Section 4, respectively. The event selection and categorisation requirements are presented in Section 5, while the estimation of the various background processes is detailed in Section 6. The theoretical and experimental uncertainties are presented in Section 7. Finally, in Section 8 the results are discussed.

2 Theoretical framework and methodology

For the studies targeting BSM contributions to the top Yukawa coupling and the effective Higgs-gluon coupling, an effective field theory framework (EFT) is chosen to parametrise possible deviations from the SM. The EFT operators probed in this note are provided by the Higgs Characterisation (HC) model [20], which is implemented in the MadGraph5_aMC@NLO generator [21]. In the heavy-top mass limit, $m_{\text{top}} \rightarrow \infty$, the CP structure of the top Yukawa coupling is inherited by the effective Higgs-gluon vertex [22]. Thus, constraints on BSM contributions will be directly set on the CP-even and CP-odd coupling strength modifiers of the effective Higgs-gluon vertex. The effective Lagrangian that describes the Higgs-gluon interaction is expressed as

$$\mathcal{L}_0^{\text{loop}} = -\frac{1}{4} \left(\kappa_{Hgg} g_{Hgg} G_{\mu\nu}^a G^{a,\mu\nu} + \kappa_{Agg} g_{Hgg} G_{\mu\nu}^a \tilde{G}^{a,\mu\nu} \right) H \,, \tag{1}$$

where κ_{Hgg} and κ_{Agg} are scale factors for the CP-even and CP-odd interactions respectively, $G_{\mu\nu}^a$ is the gluon field strength tensor, and g_{Hgg} is the effective coupling for the SM CP-even ggH interaction.

Three exemplary benchmark scenarios with different CP properties are defined in Table 1, and the distribution of the signed $\Delta\Phi_{jj}$ observable is shown in Figure 2(a) for these benchmark models.

Table 1: Definition of the three exemplary benchmark scenarios used in the ggF + 2 jets analysis. The parameter settings correspond to a CP-even (i.e. the SM hypothesis), a CP-odd, and one CP-mixed scenario.

Scenario	Parameters
CP-even (SM)	$\kappa_{Hgg} = 1, \kappa_{Agg} = 0$
CP-odd	$\kappa_{Hgg} = 0, \kappa_{Agg} = 1$
CP-mixed	$\kappa_{Hgg} = \frac{1}{\sqrt{2}}, \kappa_{Agg} = \frac{1}{\sqrt{2}}$

The analysis targeting HVV couplings in the Higgs boson production and decay uses polarisation-dependent coupling-strength scale factors defined as in Ref. [23] as

$$a_{\mathrm{L}} = \frac{g_{HV_{\mathrm{L}}V_{\mathrm{L}}}}{g_{HVV}} \, , \quad a_{\mathrm{T}} = \frac{g_{HV_{\mathrm{T}}V_{\mathrm{T}}}}{g_{HVV}} \, . \tag{2}$$

The polarisations of the vector bosons in Equation (2) are defined in the Higgs boson rest frame so that mixed-polarisation couplings $HV_{\mathrm{L}}V_{\mathrm{T}}$ do not contribute to $\sigma_{\mathrm{VBF}} \cdot \mathcal{B}_{H \to WW}$. Other BSM effects are not considered. Within the SM ($a_{\mathrm{L}} = a_{\mathrm{T}} = 1$), the HVV couplings are insensitive to polarisations.

Since polarisations depend on the measurement frame, the above description is not Lorentz invariant and as such cannot be described in the Lagrangian framework. Instead, the coupling strength modifiers a_{L} and a_{T} can be related to pseudo-observables (POs) [24]. The POs considered in the note appear as $\kappa_{VV} = \kappa_{WW} = \kappa_{ZZ}$ and $\varepsilon_{VV} = \varepsilon_{WW} = \varepsilon_{ZZ}$ in the effective Lagrangian

$$\mathcal{L} = \kappa_{VV} \left(\frac{2m_W^2}{v} HW_\mu^+ W^{-\mu} + \frac{m_Z^2}{v} HZ_\mu Z^\mu \right) - \frac{\varepsilon_{VV}}{2v} \left(2HW_{\mu\nu}^+ W^{-\mu\nu} + HZ_{\mu\nu}Z^{\mu\nu} + HA_{\mu\nu}A^{\mu\nu} \right) , \tag{3}$$

where in the SM $\kappa_{VV} = 1$ and $\varepsilon_{VV} = 0$. The universality of $\kappa_{VV} = \kappa_{WW} = \kappa_{ZZ}$ in the Lagrangian follows from assuming custodial symmetry [25], no new physics in the boson-fermion couplings Wff and Zff, and a CP-even Higgs boson with CP-conserving interactions with vector bosons. Since the study is not probing HZZ and $H\gamma\gamma$ interactions, further simplifications lead to $\varepsilon_{VV} = \varepsilon_{WW} = \varepsilon_{ZZ}$.

The coupling-strength scale factors a_{L} and a_{T} are related to the pseudo-observables via the following equations

$$a_{\mathrm{L}} = \kappa_{VV} + \Delta_{\mathrm{L}}(q_1, q_2)\varepsilon_{VV} \, , \quad a_{\mathrm{T}} = \kappa_{VV} + \Delta_{\mathrm{T}}(q_1, q_2)\varepsilon_{VV} \, . \tag{4}$$

The functions $\Delta_{\mathrm{L}}(q_1, q_2)$ and $\Delta_{\mathrm{T}}(q_1, q_2)$ depend on the momenta of electroweak bosons q_1 and q_2 (either in the production or in the decay) according to:

$$\Delta_{\mathrm{L}} = \frac{m_H^2}{2m_W^2} \frac{4q_1^2 q_2^2}{m_H^2(m_H^2 - q_1^2 - q_2^2)} \, , \quad \Delta_{\mathrm{T}} = \frac{m_H^2}{2m_W^2} \frac{m_H^2 - q_1^2 - q_2^2}{m_H^2} \, . \tag{5}$$

Based on Madgraph5_aMC@NLO simulations, we find that to a good approximation $\Delta_{\mathrm{L}}(q_1, q_2) = 0$ and $\Delta_{\mathrm{T}}(q_1, q_2) = 2$, leading to the mapping used in this note

$$\kappa_{VV} \simeq a_{\mathrm{L}} \, , \quad \varepsilon_{VV} \simeq 0.5 \cdot (a_{\mathrm{T}} - a_{\mathrm{L}}) \, . \tag{6}$$

4

This note consists of two studies. The first one places constraints on κ_{Hgg} and κ_{Agg} in the effective Hgg coupling in ggF + 2 jets Higgs production, assuming standard HVV couplings. The second study constrains the HVV parameters (a_L, a_T) and (κ_{VV}, ε_{VV}), assuming a pure CP-even Higgs state with SM Hgg coupling ($\kappa_{Hgg} = 1$, $\kappa_{Agg} = 0$). The effects of the other coupling modifications on either analysis are negligible. The constraints are derived from the rates of each production process as well as the distribution of signed $\Delta\Phi_{jj}$, whose shape dependence on the coupling modifiers is shown in Figure 2. The distribution of $\Delta\Phi_{jj}$ is displayed in the full range $[0, 2\pi]$ to capture the asymmetry for mixed CP interactions (shown in Figure 2 (a)) resulting from the interference between CP-even and CP-odd contributions[2]. Figure 2 (b) shows the dependence of $\Delta\Phi_{jj}$ on $a_L - a_T$.
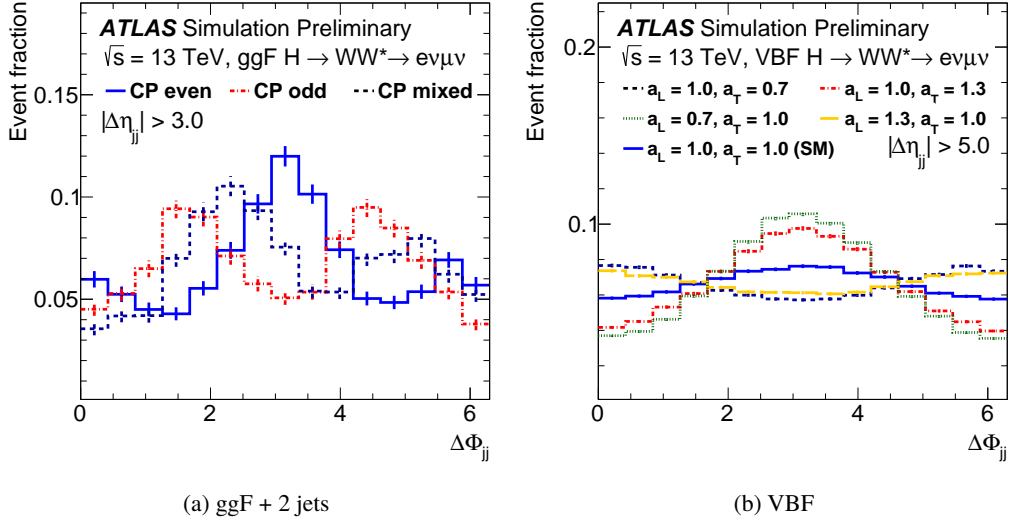

(a) ggF + 2 jets

(b) VBF

Figure 2: Distributions of the signed $\Delta\Phi_{jj}$ observable shown for (a) CP-even, CP-odd and CP-mixed benchmark models of the ggF + 2 jets production mode, and (b) various configurations of the a_L and a_T parameters in VBF events. These comparisons are performed at the generator level using the predictions of the MadGraph5_aMC@NLO v.2.4.2 + PYTHIA 8.212 generators.

3 ATLAS detector

The ATLAS detector [26] is a general-purpose particle detector used to investigate a broad range of physics processes. It includes an inner tracking detector (ID) surrounded by a thin superconducting solenoid, electromagnetic and hadronic calorimeters and a muon spectrometer (MS) incorporating three large superconducting toroid magnets with eight coils each. The ID consists of fine-granularity silicon pixel and microstrip detectors, and a straw-tube tracker. It is immersed in a 2 Tesla axial magnetic field produced by the solenoid and provides precision tracking for charged particles in the range $|\eta| < 2.5$, where η is the pseudorapidity of the particle. The straw-tube detector also provides transition radiation measurements for electron identification. The calorimeter system covers the pseudorapidity range $|\eta| < 4.9$. It is composed of sampling calorimeters with either liquid argon (LAr) or scintillator tiles as the active medium, and lead,

---

[2] As the CP-even amplitude is positive under the transformation $(\Delta\Phi_{jj} - \pi) \rightarrow -(\Delta\Phi_{jj} - \pi)$ and the CP-odd amplitude is negative under this transformation, their interference is therefore asymmetric while the individual squared amplitudes are positive.

steel, copper, or tungsten as the absorber material. The MS provides muon identification and momentum measurements for $|\eta| < 2.7$. The ATLAS detector has a two-level trigger system to select events for further analysis.

4 Data sets and Monte Carlo predictions

Candidate events in data are selected from the combined 2015 and 2016 ATLAS $\sqrt{s} = 13$ TeV pp collision dataset in which all ATLAS sub-detectors have been fully operational [27]. The corresponding total integrated luminosity [28] is 36.1 ± 0.8 fb^{-1}.

The modelling of the gluon-induced production of Higgs bosons in association with jets is realised using the MadGraph5_aMC@NLO v2.4.2 generator [29], which provides a calculation of the matrix element at next-to-leading order (NLO) precision for events with up to two additional partons in the final state. The calculations of the matrix element are based on the predictions of the HC model and the NNPDF3.0 [30] NLO parton density function (PDF) sets, while the parton shower is simulated with the Pythia 8.212 [31] generator using the A14 tune [32]. In total, three different Monte-Carlo samples are produced, corresponding to a CP-even, a CP-odd or a CP-mixed coupling between Higgs bosons and gluons, following the recommendations from Ref. [22] and using the FeynRules model HC_NLO_X0_UFO-heft [33]. Since the CP-sensitive observable $\Delta\Phi_{jj}$ is chosen to test production properties, the decay $H \rightarrow WW^* \rightarrow e\nu\mu\nu$ is modelled according to the SM.

For the measurement of the Higgs boson couplings to longitudinally and transversely polarised W bosons, the VBF production of the Higgs boson and its subsequent decays to W bosons are simulated at leading order (LO) in QCD using MadGraph5_aMC@NLO v2.4.2. For BSM signals, helicity amplitudes used in the matrix element generation of the Higgs boson production and decay are modified to account for deviations in the Higgs coupling strengths in the Higgs boson rest frame, following the prescription in Ref. [23].

For the studies of ggF + 2 jets production, the vector boson fusion production of the Higgs boson is considered as a background and an additional sample is generated to model the SM prediction for this process. In this case Powheg-Box v2 [34] is used to model the matrix element with the NNPDF3.0 NLO PDF set, while Pythia 8.212 is used to model parton shower effects. Other production and decay modes of the Higgs boson are either fixed to SM predictions (for VH production and for $H \rightarrow \tau\tau$ decay) or neglected (for $t\bar{t}H$ and $b\bar{b}H$ associated production).

The branching fractions for Higgs boson decays, calculated for a Higgs boson mass $m_H = 125.09$ GeV [35], are taken from the HDECAY program [36]. The cross section for the inclusive ggF process is computed at next-to-next-to-next-to-leading order (NNNLO) precision in QCD [37]. For the VBF production process, the cross section is computed at next-to-next-to-leading order (NNLO) precision in QCD and NLO in electroweak corrections for the VBF process using the programs VBF@NNLO [38] and HAWK [39].

Relevant sources of background include events from the production of top-quarks ($t\bar{t}$ and Wt), dibosons (WW, $WZ/WZ^{(*)}$, ZZ, $W\gamma^{(*)}$, $Z\gamma$) and single vector-bosons (W, Z/γ^*) plus jets. The production of a top-quark pair ($t\bar{t}$) is modelled using the Powheg-Box v2 generator interfaced to Pythia 8.210 with the parton shower tune A14 [32]. The matrix elements are calculated at NLO precision in QCD using the NNPDF3.0 NLO PDF set and assuming a top-quark mass of 172.5 GeV, and the hdamp parameter [40] is set to 1.5 times the top-quark mass. The $t\bar{t}$ production cross section is normalised to the predictions calculated with the Top++2.0 program to NNLO in perturbative QCD, including soft-gluon resummation

calculated to the next-to-next-to-leading logarithm (NNLL) [41]. The associated production of a single top-quark and a W boson (Wt) is generated with Powheg-Box interfaced to Pythia 6.428 for parton showering, using the Perugia2012 [42] tune. The matrix element is calculated using the CT10 [43] PDF set. The diagram removal (DR) scheme [44] is used to remove overlaps with the top-quark pair production process that occur at NLO in QCD.

The diboson production processes with $q\bar{q}$ and qg initial states and leptonic final states are simulated using Sherpa v2.2.2. The matrix elements are calculated using the NNPDF3.0 NNLO PDF set and include all relevant off-shell components. Diagrams with up to one additional emission are calculated with NLO precision in QCD, while diagrams with 2 or 3 parton emissions are described at LO accuracy [45]. The various jet-multiplicity final states are merged using the MEPS@NLO formalism [46] and a merging scale of Q_{cut} = 20 GeV. Loop-induced diboson processes that are initiated via the gg production mode are simulated at NLO in QCD using OpenLoops [47] in Sherpa 2.1.1 and the CT10 NLO PDF set. The production of dibosons with semi-leptonic decays, as well as the electroweak production of dibosons in association with two jets, are modelled using Sherpa 2.1.1 and the CT10 PDF set.

The production of a Z/γ^* boson in association with jets is modelled by Sherpa v2.2.1 with the NNPDF3.0 NNLO PDF set. Diagrams with up to 2 additional parton emissions are simulated with NLO precision in QCD, and with 3 or 4 additional parton emissions to LO accuracy. Matrix elements are merged with the Sherpa parton shower using the MEPS@NLO formalism with a merging scale of Q_{cut} = 20 GeV and the five-flavour numbering scheme (5FNS). Contributions of the electroweak production of $q\bar{q} \to Zq\bar{q}$ events are considered, in which the matrix element is generated with up to one additional emission beyond the first two partons using Sherpa v2.1.1 and the CT10 [43] PDF set. Matrix elements are merged with the Sherpa parton shower using the MEPS@NLO formalism with the merging scale set to Q_{cut} = 15 GeV. Contributions due to processes containing a single W boson produced in association with jets are estimated in a purely data-driven approach.

The MC generators, PDF sets, and programmes used to model the underlying event and parton shower (UEPS) are summarised in Table 2. The order of the perturbative prediction for each sample is also reported.

All simulated events are generated at a centre-of-mass energy of $\sqrt{s}$ = 13 TeV and then passed through the full ATLAS detector simulation [48, 49]. In addition, simulated events are overlaid with additional inelastic pp interactions that are generated with Pythia 8 [31] in order to match the pile-up conditions[3] observed in the ATLAS data recorded during the 2015 and 2016 runs of the LHC.

5 Event selection and categorisations

Candidate events consistent with the final state $H(\to WW^* \to e\nu\mu\nu)$ + 2 jets are selected. Events are triggered using single-lepton and dilepton triggers. The transverse momentum (p_T) thresholds range between 24 GeV and 26 GeV for single-electron triggers and between 20 GeV and 26 GeV for single-muon triggers, depending on the run period [50], while the dilepton trigger requires an electron with $p_T > 17$ GeV and a muon with $p_T > 14$ GeV. The trigger selection requirement corresponds to an overall efficiency of about 95% in both the ggF + 2 jets and VBF signal processes.

---

[3] An average of 13 (21) interactions per bunch crossing were observed during the 2015 (2016) run.

Table 2: Overview of the simulation tools used to generate signal and background processes, and to model the underlying event and parton shower. The PDF sets are also summarised. The prediction order (in QCD and if relevant in EW) of the total cross-section is stated for each process. Alternative event generators and configurations used to estimate systematic uncertainties are shown in parentheses.

Process	Matrix element (alternative model)	UEPS	PDF set	Prediction order for total cross-section
ggF	MG5_aMC@NLO v2.4.2 (MG5_aMC@NLO v2.4.2 + HERWIG 7.0.1)	PYTHIA 8.212	NNPDF3.0 NLO	NNNLO QCD
VBF ($a_L = 1$, $a_T = 1$)	MG5_aMC@NLO v2.4.2	PYTHIA 8.212	NNPDF3.0 NLO	NNLO QCD + NLO EW
VBF	POWHEG-BOX v2 (MG5_aMC@NLO v2.3.3 + PYTHIA 8.212) (POWHEG-BOX v2 + HERWIG 7.0.1)	PYTHIA 8.212	PDF4LHC15 NLO	NNLO QCD + NLO EW
VH	POWHEG-BOX v2	PYTHIA 8.186	PDF4LHC15 NLO	NNLO QCD + NLO EW
$t\bar{t}$	POWHEG-BOX v2 (SHERPA v2.2.1) (POWHEG-BOX v2 + HERWIG 7.0.1)	PYTHIA 8.210	NNPDF3.0 NLO	NNLO+NNLL QCD
Wt	POWHEG-BOX v2 (MG5_aMC@NLO v2.2.2 + HERWIG++) (POWHEG-BOX v2 + HERWIG++)	PYTHIA 6.428	CT10	NLO QCD
$WZ/\gamma^\star$, $ZZ/\gamma^\star$	SHERPA v2.2.2 (MG5_aMC@NLO v2.3.3 + PYTHIA 8.212)		NNPDF3.0 NNLO	NLO QCD
$W\gamma$, $Z\gamma$	SHERPA v2.2.2 (MG5_aMC@NLO v2.3.3 + PYTHIA 8.212)		NNPDF3.0 NNLO	NLO QCD
$qq, qg \rightarrow WW$	SHERPA v2.2.2 (MG5_aMC@NLO 2.3.3 + PYTHIA 8.212)		NNPDF3.0 NNLO	NLO QCD
$gg \rightarrow WW$	SHERPA v2.1.1		CT10	NLO QCD
$Z/\gamma^\star$	SHERPA v2.2.1 (MG5_aMC@NLO v2.2.2 + PYTHIA 8.186)		NNPDF3.0 NNLO	NNLO QCD

Electron candidates are reconstructed from tracks in the ID matched to clusters [51] of energy deposits in the electromagnetic (EM) calorimeter system. Electrons are required to satisfy $|\eta| < 2.47$, excluding the transition region between calorimeters, $1.37 < |\eta| < 1.52$. Muon candidates are reconstructed from combined tracks using information from both the MS and the ID. This combination is based on an overall fit using the hits of the ID track, the energy loss in the calorimeter, and the hits in the muon system. The absolute pseudorapidity of the muon candidate is required to be lower than 2.5.

Various identification requirements including calorimeter and track based isolation criteria [51, 52] are used to reduce the amount of hadrons and soft leptons stemming from heavy-flavour decays that are misidentified as prompt leptons. The electron identification efficiencies range between 88% and 94% depending on the electron p_T and $|\eta|$, while the muons identification efficiency is close to 95% over the full instrumented pseudorapidity range.

Jets are reconstructed from noise-suppressed topological clusters of energy deposits in the calorimeter system using the anti-k_t algorithm [53] with a radius of $R = 0.4$. The jet four-momentum is corrected using p_T and η dependent scale factors, which account for the calorimeter's non-compensating response, signal losses due to noise threshold effects, energy lost in passive materials, and contributions from pile-up interactions [54]. The absolute value of the pseudorapidity is required to be lower than 4.5 and

the transverse momentum has to be at least 30 GeV. To reduce the contamination from jets originating from pile-up vertices, selection requirements on two independent multivariate classifiers are applied to the selected jets. The first classifier is based on calorimeter and tracking information and is applied to jets with $p_T < 60$ GeV and $|\eta| < 2.4$ [55], while the second classifier is based on jet shapes and topological jet correlations in pile-up interactions and is applied to jets with $p_T < 50$ GeV and $|\eta| > 2.5$.

Jets containing b-hadrons are identified using the MV2c10 b-tagging algorithm [56, 57] with an operating point that has an overall efficiency of 85%, evaluated in simulated $t\bar{t}$ events. The corresponding overall rejection rate for jets originating from light-flavour hadrons or gluons is 34, while the overall rejection rate for jets containing c-hadrons is approximately 3.

The missing transverse momentum $\vec{E}_T^{\text{miss}}$ is defined as the negative vector sum of the p_T of all the selected leptons and jets, as well as all tracks compatible with the primary vertex but not associated to any of these objects [58, 59].

Ambiguities from overlapping reconstructed jet and lepton candidates are resolved as follows: If a reconstructed muon shares an ID track with a reconstructed electron, the electron is removed. Reconstructed jets are discarded if they are within a cone of size $\Delta R = 0.2$ around an electron candidate or if they have fewer than three associated tracks and are within a cone of size $\Delta R = 0.2$ around a muon candidate. Electrons and muons are removed if they are within $\Delta R = \min(0.4, 0.04 + 10 \text{ GeV}/p_T)$ of the axis of any surviving jet.

Table 3 summarises the selection requirements used to define the signal regions (SRs) of the ggF + 2 jets and VBF analyses. In order to be considered for the final analysis, candidate events must contain exactly two prompt leptons with opposite electrical charge and different lepton flavour with the higher-p_T (leading) lepton with $p_T > 22$ GeV and the subleading lepton with $p_T > 15$ GeV. The invariant mass of the dilepton system $m_{\ell\ell}$ must exceed 10 GeV. At least one of the leptons must be matched to an object that triggered the recording of the event. In case a dilepton trigger is solely responsible for the recording of an event, each lepton must be matched to one of the trigger-level objects. In addition, events must contain at least two jets passing all selection requirements. To reduce backgrounds from top-quark production, events are vetoed if they contain a b-tagged jet with a p_T larger than 20 GeV ($N_{b-\text{jet}, (p_T>20 \text{ GeV})} = 0$). The $Z(\rightarrow \tau\tau)$ + jets background is decreased by introducing a $m_{\tau\tau} < 66$ GeV selection requirement. The observable $m_{\tau\tau}$ is calculated from the four-vectors of the two charged leptons and the $\vec{E}_T^{\text{miss}}$ using the collinear approximation [60] (to reject a $Z \rightarrow \tau\tau$ hypothesis). Further selection requirements specific to the topologies of the ggF + 2 jets and VBF signal processes are used to define the two SRs. In the ggF + 2 jets analysis, the angular distance between the two leading jets ΔR_{jj} is required to be larger than 1.0, the transverse momentum of the dilepton system $p_{T,\ell\ell}$ has to exceed 20 GeV, and the $m_{\ell\ell}$ has to be below 20 GeV. In addition, the transverse mass m_T of the Higgs boson candidate must be below 150 GeV. This transverse mass is defined as $m_T = \sqrt{(E_{\ell\ell} + E_T^{\text{miss}})^2 - |\vec{p}_{T,\ell\ell} + \vec{E}_T^{\text{miss}}|^2}$ with $E_{\ell\ell} = \sqrt{|\vec{p}_{T,\ell\ell}|^2 + m_{\ell\ell}^2}$ and $\vec{p}_{T,\ell\ell}$ the combined dilepton momentum vector in the transverse plane. The selection requirements placed on $p_{T,\ell\ell}$ reduces further contributions from the Z + jets background, while the requirements on $m_{\ell\ell}$ and m_T decrease the top quark background. In the VBF analysis, an "outside lepton veto" is applied, which requires the two leptons to be within the rapidity gap spanned by the two leading jets, and a "central jet veto" rejects events with additional jets with $p_T > 20$ GeV in the rapidity gap between the two leading jets.

Boosted decision trees (BDTs) are used in both analyses to further distinguish between the signal processes and the most dominant background processes. In the ggF + 2 jets analysis, the most discriminating observables used by the BDT are the $m_{\ell\ell}$, m_T, $p_{T,\ell\ell}$ and the azimuthal angle between the two leptons $\Delta\phi_{\ell\ell}$.

In addition, the observables $\min \Delta R(\ell_1, j_i)$ and $\min \Delta R(\ell_2, j_i)$, i.e. the minimal distance between the leading and subleading lepton and the two tagging jets, are used as inputs to the BDT. The training sample of the BDT consists of the sum of simulated ggF + 2 jets events stemming from the three benchmarks models defined in Table 1 as signal, and the sum of the top quark, diboson and Z + jets processes as background. Both the input observables and the BDT response do not show any significant separation between the three CP benchmark scenarios. In the VBF analysis, the same BDT is used as described in Ref. [17], where $m_{\ell\ell}$, $\Delta\phi_{\ell\ell}$, and m_{T} are used in addition to the dijet invariant mass m_{jj}, the rapidity difference between the two leading jets Δy_{jj}, the lepton η centrality ($\sum_\ell C_\ell$ where $C_\ell = |2\eta_\ell - \sum_j \eta_j|/\Delta\eta_{jj}$ quantifies the position of a lepton relative to the two leading jets), the sum of the invariant masses of all four possible lepton–jet pairs $\sum_{\ell,j} m_{\ell,j}$, and the total transverse momentum $p_{\mathrm{T}}^{\mathrm{tot}}$, defined as the magnitude of the vectorial sum of all selected objects. The most discriminating observables used by the BDT of the VBF analysis are m_{jj} and Δy_{jj}.

Table 3: Event selection criteria used to define the signal regions for the ggF + 2 jets and VBF event categories.

	ggF + 2 jets	VBF
Preselection	Two isolated, different-flavour leptons ($\ell = e, \mu$) with opposite charge $p_{\mathrm{T}}^{\mathrm{lead}} > 22$ GeV, $p_{\mathrm{T}}^{\mathrm{sublead}} > 15$ GeV $m_{\ell\ell} > 10$ GeV $N_{\mathrm{jet}} \geq 2$	
Background rejection	$N_{b-\mathrm{jet}, (p_{\mathrm{T}} > 20\ \mathrm{GeV})} = 0$ $m_{\tau\tau} < 66$ GeV	
	$\Delta R_{jj} > 1.0$ $p_{\mathrm{T},\ell\ell} > 20$ GeV $m_{\ell\ell} < 90$ GeV $m_{\mathrm{T}} < 150$ GeV	central jet veto outside lepton veto
BDT input variables	$m_{\ell\ell}, m_{\mathrm{T}}, p_{\mathrm{T},\ell\ell}, \Delta\phi_{\ell\ell}$ $\min \Delta R(\ell_1, j_i), \min \Delta R(\ell_2, j_i)$	$m_{jj}, \Delta Y_{jj}, m_{\ell\ell}, m_{\mathrm{T}}, \Delta\phi_{\ell\ell}$ $\sum_\ell C_\ell, \sum_{\ell,j} m_{\ell,j}, p_{\mathrm{T}}^{\mathrm{tot}}$

6 Background estimation

The background contamination in the SRs originates from various processes such as the production of top-quark pairs ($t\bar{t}$), single top quarks (Wt), non-resonant dibosons (WW, WZ/γ^*, ZZ/γ^*, $W\gamma$, or $Z\gamma$), and Drell-Yan Z/γ^* (primarily in the decay $Z \to \tau\tau$). Other background contributions arise from W+jets and multi-jet production with misidentified leptons, which originate either from decays of heavy-flavour hadrons or from jets mimicking prompt-lepton signatures in the detector.

Dedicated control regions (CRs), which are exclusive to the signal region, are used to constrain the normalisation of the most dominant background processes to the data. A top CR is used to correct the normalisation of the combined $t\bar{t}$ and Wt backgrounds. A CR for $Z \to \tau\tau$ is employed to adjust the normalisation of the $Z(\to \tau\tau)$ + 2 jets production. In the ggF + 2 jets analysis, an additional WW CR is used. The definitions of the various CRs are detailed in Table 4.

Backgrounds with small contributions to the signal regions (i.e. WZ, ZZ, $W\gamma$ or $Z\gamma$) are estimated using MC simulations, while the contributions from background processes containing misidentified leptons are

Table 4: Event selection criteria used to define the various control regions for the ggF + 2 jets and VBF event categories. Stated are only the changes with respect to the signal region definitions (see Table 3).

Control region	ggF + 2 jets	VBF
top CR	$N_{b-\text{jet},(p_\text{T}>30\text{ GeV})} = 1$	$N_{b-\text{jet},(p_\text{T}>20\text{ GeV})} = 1$
$Z \to \tau\tau$ CR	$|m_{\tau\tau} - m_Z| \leq 25$ GeV	
	$p_{\text{T},\ell\ell}$ requirement is omitted	$m_{\ell\ell} < 80$ GeV
WW CR	$m_{\ell\ell} > 90$ GeV	—–
	m_T requirement is omitted	

estimated with a data-driven technique [17]. For this purpose a control sample is defined using events with one identified lepton and one lepton failing the nominal object definition requirements but passing looser requirements (referred to as anti-identified). The contribution of the misidentified lepton background to the signal region is estimated by scaling the control sample via p_T and η dependent extrapolation factors, which are defined as the ratio of the identified leptons to anti-identified leptons.

The procedure described in Section 8 is used to obtain the normalisation factors (NFs) of the dominant background processes from a combined SR + CR fit to data, where each background normalisation is correlated across all regions. In the ggF + 2 jets analysis, the normalisations of the top quark, Z + jets and WW backgrounds are determined simultaneously. The WW CR has approximately equal contributions from WW and top processes, so there is a moderate anti-correlation between the NFs of the WW and top-quark backgrounds. The WW CR nonetheless constrains the sizeable WW modelling uncertainty. In the VBF analysis, the normalisations of the top quark and Z + jets backgrounds are determined following the strategy described in Ref. [17].

Exemplary results are summarised in Table 5 separately for the ggF + 2 jets and VBF analyses. The NFs for the ggF + 2 jets analysis correspond to a scan over $\kappa_{Agg}/\kappa_{Hgg}$ using both shape and rate information in the likelihood fit. The NFs for the VBF analysis are obtained from a scan over a_L exploiting both shape and rate information. Both sets of normalisation factors differ slightly depending on which (B)SM model is tested, but are consistent within their total uncertainties. The normalisation factors of the Z+jets background are affected by residual misalignments in the ID which distort the measurements of the track parameters for particles originating from secondary vertices, e.g. leptons from τ decays [17].

Table 5: Post-fit NFs and their uncertainties for the Z+jets, top and WW backgrounds. The NFs for the ggF + 2 jets analysis correspond to the scan over $\kappa_{Agg}/\kappa_{Hgg}$ using both shape and rate information in the likelihood fit. The NFs for the VBF analysis are obtained from a scan over a_L exploiting both shape and rate information. Both sets of normalisation factors differ slightly depending on which (B)SM model is tested, but are consistent within their total uncertainties.

Phase space	$\text{NF}^{Z+\text{jets}}$	NF^{top}	NF^{WW}
ggF + 2 jets	$0.85^{+0.09}_{-0.09}$	$1.05^{+0.06}_{-0.05}$	$1.0^{+0.7}_{-0.4}$
VBF	$0.94^{+0.21}_{-0.18}$	$1.00^{+0.06}_{-0.05}$	—–

7 Systematic uncertainties

The effects of the systematic uncertainties on the expected signal and background yields in the various signal and control regions are evaluated following the procedures in Ref. [17]. In adddition, the effects of the uncertainties on the shape of the $\Delta\Phi_{jj}$ and BDT response distributions are considered. They are evaluated by individually comparing the nominal distribution to those corresponding to up and down variations of a particular uncertainty.

The sources of uncertainty are grouped into two categories: experimental and theoretical. The dominant experimental uncertainties for both analyses are related to the b-tagging efficiency [61], the jet energy scale and resolution [62], the modelling of pile-up activity, and the estimation of the misidentified-lepton background [17]. Smaller uncertainties are due to the lepton momentum scale and resolution, the lepton identification and isolation criteria [51, 52, 63], the missing transverse momentum measurement [64], and the luminosity measurement [65]. The luminosity uncertainty is only applied to those processes that are normalised to theoretical predictions.

Theoretical uncertainties are assessed by comparing nominal and alternative event generators and UEPS models, as indicated in Table 2. The modelling uncertainties on the $t\bar{t}$ background are derived as follows: to assess potential differences in the matching between the matrix element and parton shower, the predictions of the nominal generator setup are compared to those of the SHERPA v2.2.1 generator. Parton shower modelling uncertainties are derived by replacing PYTHIA 8.210 by HERWIG 7.0.1 and comparing the corresponding yields and shapes to those of the nominal setup. The uncertainty due to neglected higher orders in QCD is estimated by simultaneously shifting up (down) the renormalisation and factorisation scales μ_R and μ_F by a factor of 2 (0.5) as well as setting the hdamp parameter to 1.0 and 3.0 times the top quark mass. For the Wt production, uncertainties on the matching between the matrix element and parton shower are evaluated by comparing the predictions of POWHEG-BOX v2 + HERWIG++ to those of MG5_aMC@NLO v2.2.2 + HERWIG++, while the parton shower model uncertainties are estimated by comparing POWHEG-BOX v2 + PYTHIA 6.428 to POWHEG-BOX v2 + HERWIG++. In addition, the nominal configuration of the Wt process is compared to an alternative approach in which the diagram subtraction scheme is used instead of the DR scheme. The uncertainty due to neglected higher orders in QCD is estimated by shifting the renormalisation and factorisation scales up (down) by a factor of 2 (0.5) with respect to the nominal value.

The modelling uncertainties on the production of vector bosons with jets are evaluated as follows: For the production of $WZ/\gamma^\star$, $ZZ/\gamma^\star$, WW, $W\gamma$, and $Z\gamma$ the predictions of the SHERPA v2.2.2 generator are compared to those of the MG5_aMC@NLO 2.3.3 + PYTHIA 8.212 generators, which provide NLO precision in QCD for the simulation of production modes with up to one parton in addition to the diboson system [45]. In this generator setup, the FxFx merging is used to remove overlaps between the partonic configuration produced during the simulation of the matrix element and the parton shower using a merging scale of 20 GeV. For the predictions of the processes $WZ/\gamma^\star$, $ZZ/\gamma^\star$, and WW, variations of the matching scale are also considered, where the nominal value, 20 GeV, is shifted up (down) to 30 GeV (15 GeV). For the Z + jets background, matrix element and parton shower variations are both accounted for by comparing the predictions of the SHERPA v2.2.1 generator to those of MG5_aMC@NLO v2.2.2 + PYTHIA 8.186, which provides matrix elements at LO accuracy with up to four final-state partons. In addition, the effects of QCD factorisation and renormalisation scale variations are considered by individually shifting up (down) μ_R and μ_F by a value of 2 (0.5). Six combinations are considered: $(\mu_R, \mu_F) = (0.5, 0.5)$, $(0.5, 1.0)$, $(1.0, 0.5)$, $(1.0, 2.0)$, $(2.0, 1.0)$, and $(2.0, 2.0)$. The final QCD scale uncertainty is obtained as the largest up (down) variation with respect to the central value $(\mu_R, \mu_F) = (1.0, 1.0)$.

The modelling uncertainties on the ggF and VBF production modes of the Higgs boson are evaluated as follows: Parton shower model uncertainties for the ggF + 2 jets process are determined by comparing the predictions of the nominal generator configuration to that of the MG5_aMC@NLO v2.4.2 + HERWIG 7.0.1 generators. QCD scale variations have been determined for the ggF + 2 jets and VBF processes in the same way as for the vector boson plus jets backgrounds. Uncertainties on the ggF and VBF production cross sections and jet bin migration effects for the ggF process have been accounted for following the recommendations from Ref. [37]. In the ggF + 2 jet analysis, further uncertainties are considered on the VBF background. Uncertainties based on the matching of the matrix element and the parton shower are evaluated by comparing the predictions of POWHEG-BOX v2 + PYTHIA 8.212 to the predictions of MG5_aMC@NLO v2.3.3 + PYTHIA 8.212, while parton shower model uncertainties are derived comparing the predictions of POWHEG-BOX v2 + PYTHIA 8.212 to those of POWHEG-BOX v2 + HERWIG 7.0.1.

In addition, PDF model uncertainties are evaluated on the signal processes and all relevant backgrounds by comparing the predictions of the nominal PDF set to those of the CT14 and MMHT2014 PDF sets and comparing the difference to the root mean square spread of the NNPDF3.0 replica sets. The larger of the two is taken as the uncertainty. The uncertainties on the signal processes have been evaluated based on the SM hypotheses and are extrapolated to the various BSM scenarios assuming that QCD scale, PDF and parton shower model effects factorise with the modulations of the $\Delta\Phi_{jj}$ shape and cross sections due to BSM contributions. These modelling uncertainties are treated as fully correlated between the SM and BSM hypotheses.

In the VBF study, an additional uncertainty is applied to the dijet invariant mass distribution of all backgrounds, following [17].

The most significant theoretical uncertainties are related to the modelling of the top quark and *WW* backgrounds and the ggF process. Table 7 and Table 11 rank the various uncertainties and show their impact on the studies of the ggF + 2 jets and VBF processes. Both studies are dominated by statistical uncertainties. Some systematic uncertainties have a significant impact on the determination of the the the post-fit normalisation factors (presented in Table 5). In the ggF + 2 jets analysis, significant anti-correlations have been found between the normalisation of the top quark background and the uncertainty on the *b*-tagging efficiency. The normalisation factor of the *WW* background is significantly anti-correlated with both the uncertainty on the *b*-tagging efficiency and the QCD scale uncertainty on the *WW* backgrounds, while the normalisation factor of the *Z*+jets background is significantly anti-correlated with the jet energy scale uncertainties. In the VBF analysis, no significant anti-correlations are observed between the normalisation factors and the various uncertainties.

8 Results

A maximum likelihood (ML) fit is used for the statistical interpretation of the results from both the ggF + 2 jets and VBF analyses. Fits are simultaneously performed on all considered SRs and CRs in order to constrain the normalisation of backgrounds and nuisance parameters (NPs) describing the systematic uncertainties. Individual sources of systematic uncertainty are considered uncorrelated, while the correlation of a given systematic uncertainty is maintained across processes and channels. Due to the presence of bins with low event yields, all the NPs describing the systematic uncertainties are incorporated into the fit using a log-normal constraint, such that expected event counts remain positive for all values of the corresponding NPs. Asimov datasets have been used to study the expected performance of each fit.

Parameter morphing [66, 67] is used to interpolate and extrapolate from a small set of κ_{Hgg} and κ_{Agg} (or a_L and a_T) coupling benchmarks to a large variety of coupling scenarios. The input distributions to the morphing are normalised to their expected cross sections.

The final results are obtained by applying the maximum likelihood procedure individually to each coupling parameter hypothesis, where the background prediction is only affected by changes to nuisance parameters in the minimization. A negative log-likelihood (NLL) curve is constructed as a function of the relevant coupling parameters. The best estimate for the parameter of interest is obtained at the point where the NLL curve reaches its minimum. In addition, central confidence intervals are determined from the appropriate deviation of the NLL from its minimum.

8.1 ggF + 2 jets category

The ML fits that constrain BSM effects in the effective Higgs-gluon coupling use the distribution of the signed $\Delta\Phi_{jj}$ observable as input, divided into 12 categories. These 12 different categories are obtained by splitting the signal region into three BDT score intervals times four $|\Delta\eta_{jj}|$ intervals[4]. The bin boundaries for the BDT score and $|\Delta\eta_{jj}|$ intervals that define the categories are $[0.1, 0.4, 0.7, 1.0]$ and $[0.0, 1.0, 2.0, 3.0, \infty]$, respectively. Finally, the event yields from the top, $Z \to \tau\tau$ and WW CRs, as well as the event yields within the low-BDT-score intervals $w_\mathrm{BDT} \in [-1.0, -0.3]$ and $w_\mathrm{BDT} \in [-0.3, 0.1]$ in each $|\Delta\eta_{jj}|$ region are included in the ML fit. These regions provide constraints on the normalisations of the top quark, Z+jets and WW+jets backgrounds, which are free to float in the fit, as well as on the b-tagging uncertainties. All other background contributions are set to their respective SM predictions, but are allowed to vary within their uncertainties.

For the measurement of the signal strength parameter for ggF + 2 jets events $\mu^{\mathrm{ggF+2jets}}$, the ML fit uses a distribution that is built from the same five BDT-score and four $|\Delta\eta_{jj}|$ intervals as those used for the studies of the effective Higgs-gluon coupling. In addition to this distribution, the event yields from the top, $Z \to \tau\tau$, and WW CRs are included in the fit. The normalisations of the VBF, top quark, Z+jets, and WW+jets backgrounds are free to float in the fit, while all other background contributions are set to their respective SM predictions, but are allowed to vary within their uncertainties.

Four different fits are performed in the ggF + 2 jets event category:

- The signal strength parameter $\mu^{\mathrm{ggF+2jets}}$ for the ggF + 2 jets signal process is constrained. This parameter is defined as the ratio of the measured signal yield to that predicted by the SM.

- In order to constrain BSM effects in the effective Higgs-gluon coupling, $\kappa_{Agg}/\kappa_{Hgg}$ is scanned as one parameter. Two different configurations are used in the ML procedure:
    - The normalisation of the signal process is unconstrained such that the analysis only exploits the shape information of the fit input distribution to distinguish between the different CP scenarios.
    - The signal normalisation is constrained to the model predictions. Thus both the shape and rate information of the signal process are considered.

---

[4] The split into BDT score regions aims to maximize the signal over background ratio, while the split into $|\Delta\eta_{jj}|$ regions is motivated by the fact that the separation between the various CP hypotheses for the signed $\Delta\Phi_{jj}$ distribution increases with higher $|\Delta\eta_{jj}|$ values.

Using both shape and rate information in the fit increases the sensitivity to distinguish between the various benchmark points. However, the rate can be affected by multiple BSM effects, while the shape isolates CP-dependent variations.

- A simultaneous fit of the coupling strength scale factors κ_{Hgg} and κ_{Agg} is performed. This study exploits both shape and rate information.

The post-fit distribution of the inputs to the signal strength parameter $\mu^{\text{ggF+2jets}}$ determination is depicted in Figure 3. The normalised $\Delta\Phi_{jj}$ distribution in the various event categories of the ggF +2 jets signal region is depicted in Figure 4. Events are weighted by $\ln(1 + N_{\text{S}}/N_{\text{B}})$, where N_{S} (N_{B}) is the post-fit signal (background) event yield for each event category. This distribution is presented for the minimum of the NLL curve from the fit configuration that exploits both shape and rate information. The post-fit event yields in the signal and the various control regions are presented in Table 6.
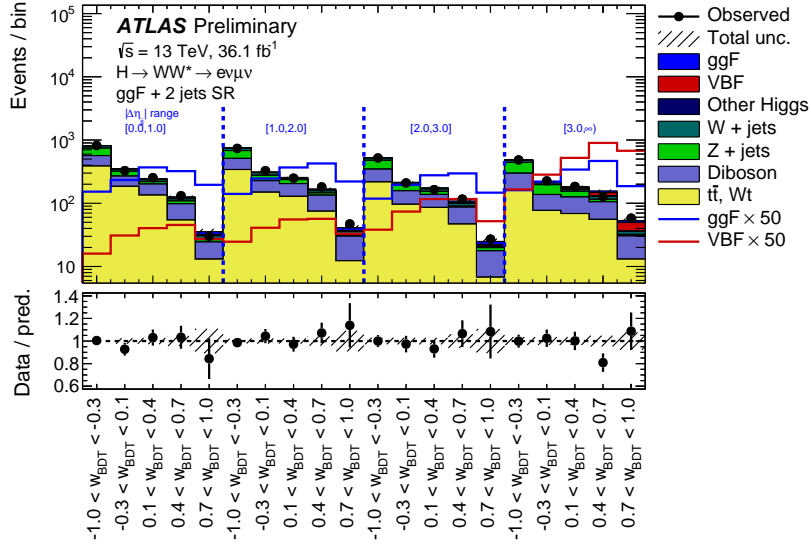
Figure 3: Post-fit distribution of the BDT response observable presented in the four $|\Delta\eta_{jj}|$ categories of the ggF +2 jets signal region, with signal and background yields fixed from the fit to $\mu^{\text{ggF+2jets}}$. Data-to-simulation ratios are shown at the bottom of the plot. The shaded areas depict the total uncertainty. The distributions of the ggF + 2 jets and VBF processes are overlaid after their respective contributions have been multiplied by 50.

The signal strength parameter of the ggF + 2 jets process is found to be $\mu^{\text{ggF+2jets}} = 0.5 \pm 0.4(\text{stat.})^{+0.7}_{-0.6}(\text{syst.})$ and is consistent with the SM predictions. The observed and expected likelihood curves corresponding to scans over $\kappa_{Agg}/\kappa_{Hgg}$ are presented in Figure 5. The values of the NLL are evaluated in steps of $\Delta(\kappa_{Agg}/\kappa_{Hgg}) = 0.2$, and the minima of all fits are consistent with zero, i.e. the SM hypothesis. If only the shape information is used, the data are not sensitive enough to provide 68% confidence level (CL) intervals on $\kappa_{Agg}/\kappa_{Hgg}$. The ML fit configuration that uses both shape and rate information provides a best-fit value of $\kappa_{Agg}/\kappa_{Hgg} = 0.0 \pm 0.4(\text{stat.}) \pm 0.3(\text{syst.})$ for both the fits on data and Asimov data. The observed sensitivity is slightly worse than the expected sensitivity due to a lower than expected signal yield (consistent with a signal strength parameter below unity). Hence, the fit to this data set does not provide a 95% CL interval. The relative impact of the main uncertainties on $\kappa_{Agg}/\kappa_{Hgg}$ is presented in Table 7.

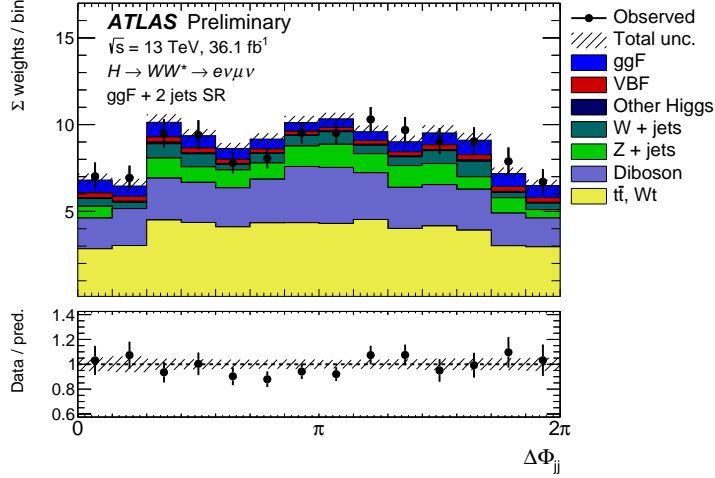As EFTs are only valid for small variations around the SM, it is more natural to express the CP-

Figure 4: The weighted $\Delta\Phi_{jj}$ post-fit distribution in the ggF +2 jets signal region, with signal and background yields fixed from the fit to $\kappa_{Agg}/\kappa_{Hgg}$ using shape and rate information. Data-to-simulation ratios are shown at the bottom of the plot. The shaded areas depict the total uncertainty.

Table 6: Post-fit event yields in the signal and control regions obtained from the study of the signal strength parameter $\mu^{\mathrm{ggF+2jets}}$. The quoted uncertainties include the theoretical and experimental systematic sources and those due to sample statistics.

Process	Top CR	WW CR	$Z \to \tau\tau$ CR	SR
ggF + 2 jets	20 ± 20	< 0.1	10 ± 10	60 ± 80
ggF + 0/1 jets	4 ± 1	< 0.1	3 ± 1	40 ± 20
VBF	8 ± 1	< 0.1	7 ± 1	70 ± 10
Other Higgs	6.0 ± 0.3	2.4 ± 0.1	20 ± 4	26 ± 1
$WZ, ZZ, W\gamma, Z\gamma$	40 ± 30	100 ± 30	120 ± 50	240 ± 80
$t\bar{t}, Wt$	17800 ± 200	3100 ± 500	390 ± 60	2300 ± 300
W + jets	600 ± 200	140 ± 30	90 ± 20	390 ± 80
WW	180 ± 80	1400 ± 500	200 ± 70	1200 ± 400
Z + jets	220 ± 30	16 ± 3	1960 ± 70	1000 ± 100
Observed	18886	4778	2800	5209

even and CP-odd coupling strength parameters as differences with respect to their SM predictions $\Delta\kappa_{Hgg} = \kappa_{Hgg}^{\mathrm{Measured}} - \kappa_{Hgg}^{\mathrm{SM}}$ and $\Delta\kappa_{Agg} = \kappa_{Agg}^{\mathrm{Measured}} - \kappa_{Agg}^{\mathrm{SM}}$ with $\kappa_{Hgg}^{SM} = 1$ and $\kappa_{Agg}^{SM} = 0$. The 68% and 95% CL two-dimensional likelihood contours of the simultaneous scan over the CP-even and CP-odd coupling strength parameters κ_{Hgg} and κ_{Agg} are presented in Figure 6. The best-fit value observed in the data is consistent with the SM predictions within the 68% CL, while $|\kappa_{Hgg}|$ values above 1.6 and $|\kappa_{Agg}|$ values above 1.1 are excluded at 95% CL.
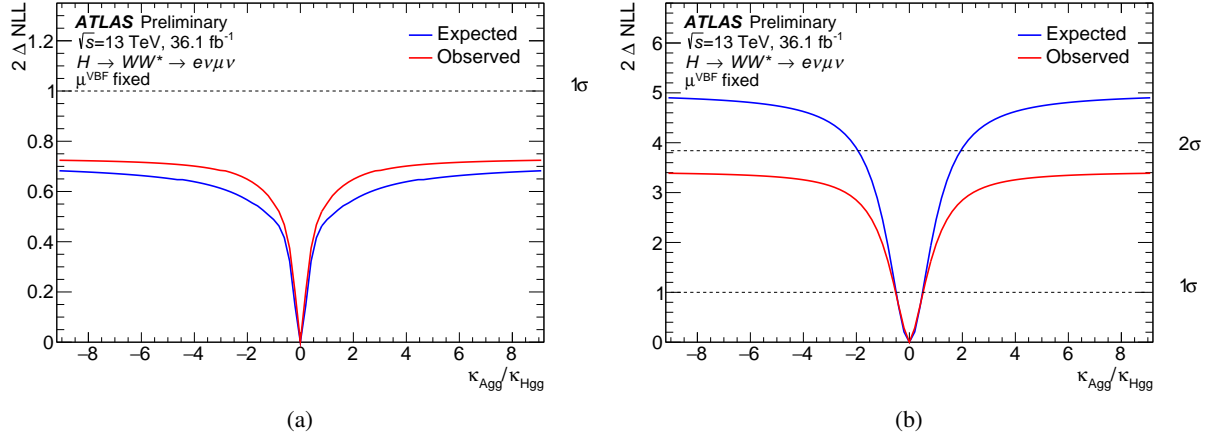
Figure 5: Expected and observed likelihood curves for scans (a) over $\kappa_{Agg}/\kappa_{Hgg}$ where only the shape is taken into account in the fit, and (b) over $\kappa_{Agg}/\kappa_{Hgg}$ when both shape and normalisation are used.

Table 7: Breakdown of the main contributions to the total uncertainty on $\kappa_{Agg}/\kappa_{Hgg}$ based on the fit that exploits both shape and rate information. Individual sources of systematic uncertainty are grouped into either the theoretical or the experimental uncertainty. The sum in quadrature of the individual components differs from the total uncertainty due to correlations between the components.

Source	$\Delta\left(\kappa_{Agg}/\kappa_{Hgg}\right)$
Total data statistical uncertainty	0.4
SR statistical uncertainty	0.33
CR statistical uncertainty	0.10
MC statistical uncertainty	0.14
Total systematic uncertainty	0.28
Theoretical uncertainty	0.23
Top quark bkg.	0.15
ggF signal	0.14
$WZ, ZZ, W\gamma, Z\gamma$ bkg.	0.06
WW bkg.	0.06
Z/γ^* bkg.	0.016
VBF bkg.	0.015
Experimental uncertainty	0.21
b-tagging	0.16
Modelling of pile-up	0.10
Jets	0.07
Misidentified leptons	0.04
Luminosity	0.034
Total	0.5
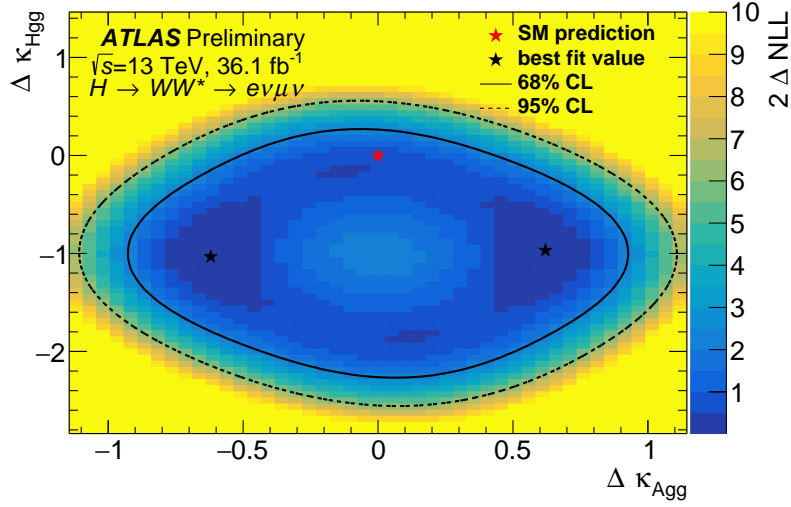
Figure 6: 68% and 95% CL two-dimensional likelihood contours of the CP-even and CP-odd coupling parameters $\Delta\kappa_{Hgg}$ and $\Delta\kappa_{Agg}$. The minima are represented by black stars, while the SM value is shown as a red star.

8.2 VBF category

To constrain the polarisation-dependent coupling strength scale factors in the VBF production process, the signal region and background control regions defined in Tables 3 and 4 are used as inputs to the ML fit. In the signal region, the distribution of the signed $\Delta\Phi_{jj}$ observable is used in the four categories defined by the BDT-score intervals $[-1, 0.26, 0.61, 0.86, 1]$, following Ref. [17]. The first (last) interval corresponds to the enhanced background (signal) phase space region. No shape information is used in the control regions.

Several types of fits are performed in the VBF event category with both (a_L, a_T) and $(\kappa_{VV}, \varepsilon_{VV})$ parametrisations:

- One dimensional fits are performed

  - using only the shape dependence of the fit input distribution on the selected parameter of interest (with the exception of a_L and κ_{VV} due to their small significance), with the other parameter fixed to its SM value;"

  - exploiting both shape and rate information, fixing one parameter to its SM value.

  The parameters a_L and κ_{VV} are more sensitive to the total event yields because the longitudinal polarisation vectors of the massive gauge bosons are proportional to energy and can give large enhancements to the total cross section. The parameters a_T and ε_{VV}, on the other hand, are sensitive to the shape of $\Delta\Phi_{jj}$. The kinematic distributions of the two tagging jets are related to the intrinsic structure of the Higgs boson production vertex and carry information about the polarisation of the fusing gauge bosons.

- Fits are performed to one parameter with the other being profiled. In these fits, both parameters may vary independently in order to probe them in a model-independent way.

Table 8: Post-fit event yields in the signal and control regions obtained from a scan over ε_{VV} exploiting both shape and rate information. The quoted uncertainties include the theoretical and experimental systematic sources and those due to sample statistics.

Process	Top CR	$Z \to \tau\tau$ CR	SR
VBF	3.2 ± 2.2	2.6 ± 1.8	34 ± 22
ggF	3.9 ± 1.7	2.4 ± 1.0	28 ± 12
Other Higgs	1.5 ± 0.2	6.2 ± 0.4	6.0 ± 0.4
$WZ, ZZ, W\gamma, Z\gamma$	14.3 ± 1.8	20.8 ± 3.3	83 ± 11
$t\bar{t}, Wt$	7400 ± 100	53 ± 7	1220 ± 100
W + jets	190 ± 40	23.0 ± 2.4	115 ± 27
WW	51 ± 6	21.8 ± 2.9	360 ± 70
Z + jets	54 ± 10	370 ± 24	320 ± 70
Observed	7668	501	2164

Figure 7 depicts the weighted $\Delta\Phi_{jj}$ distribution in all categories of the VBF signal region. Events are weighted by $\ln(1 + N_S/N_B)$ in their corresponding event category. The results of the likelihood scans on the expected and observed distributions are given in Figure 8. The scan over a_L (a_T) is shown in the upper (lower) panel. Both scans have been performed in two configurations: the LLH curves shown in Figure 8 (a) and (c) are the results of the fit in which both shape and normalisation of the signal are taken into account, while the LLH curves in Figure 8 (b) are obtained using only the shape information. The largest sensitivity to a_L stems from the rate information. The asymmetry of the fit results from the asymmetric behaviour of the cross section with respect to the changes in parameters (see Ref. [23]). The expected sensitivity to a_T comes predominantly from the shape information, as the likelihood ratio increases only slightly when adding the normalisation information. The resulting best-fit values and their uncertainties computed at 68% CL are presented in Table 9. All measurements are consistent with the SM expectations. The dominant sources of uncertainty are related to the limited data yields and to the modelling uncertainties on the top-quark and WW backgrounds.

Table 9: Best-fit values and their uncertainties as obtained from the shape-only and shape-plus-rate likelihood fits to the Asimov dataset and to ATLAS data. The results of both shape-only and shape+rate fits for a_L and a_T are shown. Results of fits to one parameter with the other one fixed or profiled are presented.

| Type	exp.	obs.
a_L shape-only fit ($a_T = 1$)	–	–
a_T shape-only fit ($a_L = 1$)	$1.00 \pm 0.5(\text{stat.})^{+0.35}_{-0.39}(\text{syst.})$	$1.27^{+0.8}_{-0.4}(\text{stat.})^{+0.35}_{-0.27}(\text{syst.})$
a_L shape + rate fit ($a_T = 1$)	$1.00^{+0.08}_{-0.10}(\text{stat.})^{+0.08}_{-0.13}(\text{syst.})$	$0.90^{+0.10}_{-0.13}(\text{stat.})^{+0.09}_{-0.19}(\text{syst.})$
a_T shape + rate fit ($a_L = 1$)	$1.00^{+0.36}_{-0.49}(\text{stat.})^{+0.22}_{-0.32}(\text{syst.})$	$1.18^{+0.26}_{-0.31}(\text{stat.})^{+0.14}_{-0.16}(\text{syst.})$
a_L shape + rate fit (a_T profiled)	$1.00^{+0.08}_{-0.10}(\text{stat.})^{+0.08}_{-0.13}(\text{syst.})$	$0.91^{+0.10}_{-0.18}(\text{stat.})^{+0.09}_{-0.18}(\text{syst.})$
a_T shape + rate fit (a_L profiled)	$1.00^{+0.38}_{-0.5}(\text{stat.})^{+0.22}_{-0.43}(\text{syst.})$	$1.16 \pm 0.4(\text{stat.})^{+0.4}_{-0.3}(\text{syst.})$
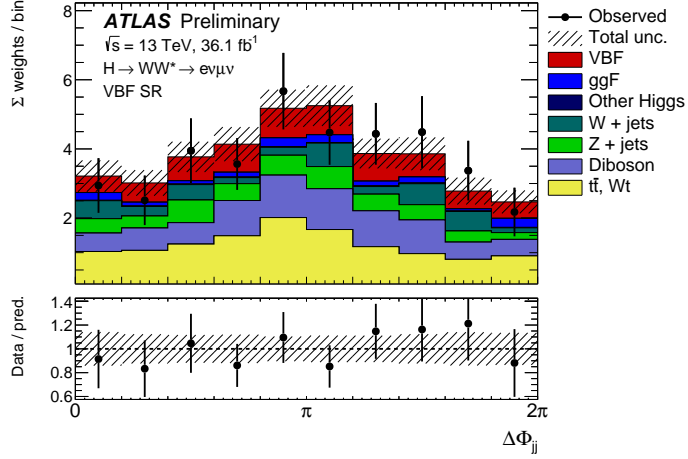
Figure 7: The weighted $\Delta\Phi_{jj}$ distribution in the VBF signal region, with signal and background yields fixed from the fit to ε_{VV} using shape and rate information. Data-to-simulation ratios are shown at the bottom of the plot. The shaded areas depict the total uncertainty.

The results of the ML scans of pseudo-observables are shown in Table 10, with the uncertainty breakdown given in Table 11. Figure 9 shows the expected and observed likelihood curves for scans over one pseudo-observable with the other one profiled. Both shape and rate information are employed.

(a) a_L shape+rate fit with $a_T = 1$

(b) a_T shape-only fit with $a_L = 1$

(c) a_T shape+rate fit with $a_L = 1$
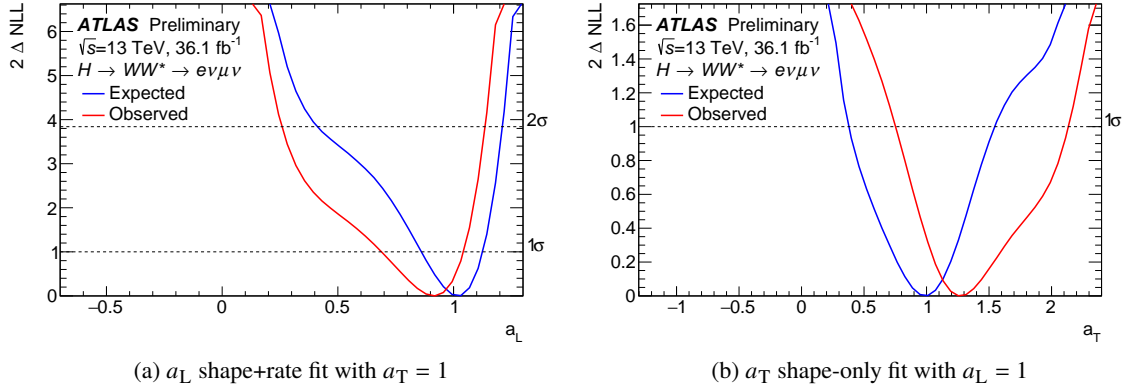
Figure 8: Likelihood scans over the longitudinally (a) and transversally (b, c) polarised couplings. Both normalisation and shape (a,c) and shape-only (b) fits are shown. All relevant experimental and modelling systematic uncertainties are considered in the fit.

(a) κ_{VV} shape+rate with profiled ε_{VV}

(b) ε_{VV} shape+rate fit with profiled κ_{VV}
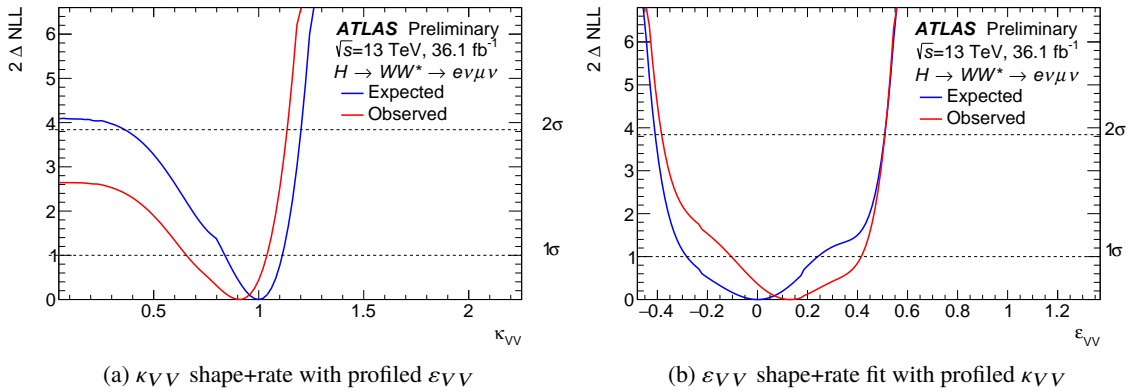
Figure 9: Likelihood scans over κ_{VV} (a) and ε_{VV} (b) with the other parameter profiled. The fits are performed using both shape and rate information. All relevant experimental and theoretical systematic uncertainties are considered in the fit.

Table 10: Best-fit values and their uncertainties as obtained from the shape-only and shape-plus-rate likelihood fits to the Asimov dataset and to ATLAS data. The results of both shape-only and shape+rate fits for ε_{VV} and κ_{VV} are shown. Results of fits to one parameter with the other one fixed or profiled are presented.

Type	exp.	obs.
κ_{VV} shape-only fit ($\varepsilon_{VV} = 0$)	–	–
ε_{VV} shape-only fit ($\kappa_{VV} = 1$)	$0.00^{+0.23}_{-0.25}$ (stat.)$^{+0.17}_{-0.20}$(syst.)	$0.14^{+0.39}_{-0.22}$(stat.)$^{+0.18}_{-0.13}$(syst.)
κ_{VV} shape + rate fit ($\varepsilon_{VV} = 0$)	$1.00^{+0.08}_{-0.10}$(stat.)$^{+0.08}_{-0.12}$(syst.)	$0.91^{+0.09}_{-0.12}$(stat.)$^{+0.09}_{-0.17}$(syst.)
ε_{VV} shape + rate fit ($\kappa_{VV} = 1$)	$0.00^{+0.18}_{-0.24}$(stat.)$^{+0.10}_{-0.13}$(syst.)	$0.09^{+0.13}_{-0.16}$ (stat.)$^{+0.06}_{-0.07}$(syst.)
κ_{VV} shape + rate fit (ε_{VV} profiled)	$1.00^{+0.08}_{-0.10}$(stat.)$^{+0.08}_{-0.12}$(syst.)	$0.90^{+0.10}_{-0.18}$(stat.)$^{+0.09}_{-0.16}$(syst.)
ε_{VV} shape + rate fit (κ_{VV} profiled)	$0.00^{+0.22}_{-0.24}$ (stat.)$^{+0.11}_{-0.15}$(syst.)	$0.13^{+0.28}_{-0.20}$ (stat.)$^{+0.08}_{-0.10}$(syst.)

Table 11: The contributions of the individual systematic uncertainties, together with the data statistical uncertainties in the one dimensional fit for the Higgs pseudo-observables for electroweak-boson polarisation in the VBF $H \rightarrow WW$ channel. Both shape and rate informations are exploited in the fit. The theoretical and experimental uncertainties are subdivided further into categories.

Source	$\Delta\kappa_{VV}$	Source	$\Delta\varepsilon_{VV}$
Total data statistical uncertainty	0.11	Total data statistical uncertainty	0.14
SR data statistical uncertainty	0.10	SR data statistical uncertainty	0.14
CR data statistical uncertainty	0.019	CR data statistical uncertainty	0.011
MC statistical uncertainty	0.035	MC statistical uncertainty	0.036
Total systematic uncertainty	0.12	Total systematic uncertainty	0.066
Theoretical uncertainty	0.10	Theoretical uncertainty	0.050
Top quark bkg.	0.072	WW bkg.	0.036
WW bkg.	0.062	Top quark bkg.	0.039
ggF bkg.	0.022	ggF bkg.	0.013
Z/γ^* bkg.	0.017	Z/γ^* bkg.	0.012
VBF signal	0.019	VBF signal	0.010
Experimental uncertainty	0.050	Experimental uncertainty	0.024
b-tagging	0.014	b-tagging	0.010
Jet	0.026	Modelling of pile-up	0.022
Misidentified leptons	0.041	Jet	0.018
Luminosity	0.011	Misidentified leptons	0.010
Total	0.17	Total	0.16
(a) κ_{VV} fit; $\varepsilon_{VV} = 0$		(b) ε_{VV} fit; $\kappa_{VV} = 1$	

9 Conclusion

This note presents constraints on the CP structure of gluon-fusion Higgs boson production and on the polarisations of the vector bosons in the HVV coupling. The results are obtained using $H(\to WW^* \to e\nu\mu\nu)jj$ final states based on 36.1 fb^{-1} of proton–proton collisions at $\sqrt{s} = 13$ TeV recorded by the ATLAS detector at the LHC in 2015–2016. Total event yields as well as shapes of selected kinematical distributions in the signal and control regions are exploited.

The signal strength parameter for the ggF + 2 jets Higgs boson production was found to be $\mu^{\text{ggF+2jets}} = 0.5 \pm 0.4(\text{stat.})^{+0.7}_{-0.6}(\text{syst.})$. The ratio of the CP-odd to CP-even coupling strength scale factors of the effective Higgs-gluon vertex was constrained to $\kappa_{Agg}/\kappa_{Hgg} = 0.0 \pm 0.4(\text{stat.}) \pm 0.3(\text{syst.})$ using both shape and rate information.

The reported results for the VBF Higgs boson production mode include constraints on coupling-strength form factors to longitudinally and transversely polarised W and Z bosons. In one-dimensional ML fits (where the other parameter was set to its SM value) shape only information is sufficient to constrain the coupling to transversely polarised bosons, a_T, while to constrain a_L the information on the rates significantly improves the sensitivity. Profiling the other coupling-strength scale factor results in: $a_{\text{L}} = 0.91^{+0.10}_{-0.18}(\text{stat.})^{+0.09}_{-0.18}(\text{syst.})$ and $a_{\text{T}} = 1.16 \pm 0.4(\text{stat.})^{+0.4}_{-0.3}(\text{syst.})$, while $a_{\text{L}} = 1.00^{+0.08}_{-0.10}(\text{stat.})^{+0.08}_{-0.13}(\text{syst.})$ and $a_{\text{T}} = 1.00^{+0.38}_{-0.5}(\text{stat.})^{+0.22}_{-0.43}(\text{syst.})$ are expected.

With an approximate mapping to pseudo-observables the following constraints are obtained: $\kappa_{VV} = 0.90^{+0.10}_{-0.18}(\text{stat.})^{+0.09}_{-0.16}(\text{syst.})$ and $\epsilon_{VV} = 0.13^{+0.28}_{-0.20}(\text{stat.})^{+0.08}_{-0.10}(\text{syst.})$, while $\kappa_{VV} = 1.00^{+0.08}_{-0.10}(\text{stat.})^{+0.10}_{-0.13}(\text{syst.})$ and $\epsilon_{VV} = 0.00^{+0.22}_{-0.24}(\text{stat.})^{+0.11}_{-0.15}(\text{syst.})$ are expected. In this parametrisation the sensitivity to the on-shell coupling κ_{VV} is affected by the event yields, while the off-shell coupling ϵ_{VV} is sensitive to both shape and rate information.

All measurements are consistent with the expectations for the SM Higgs boson.

Appendix

Auxiliary figures in the gluon fusion (ggF + 2 jets) and vector-boson fusion (VBF) analyses.
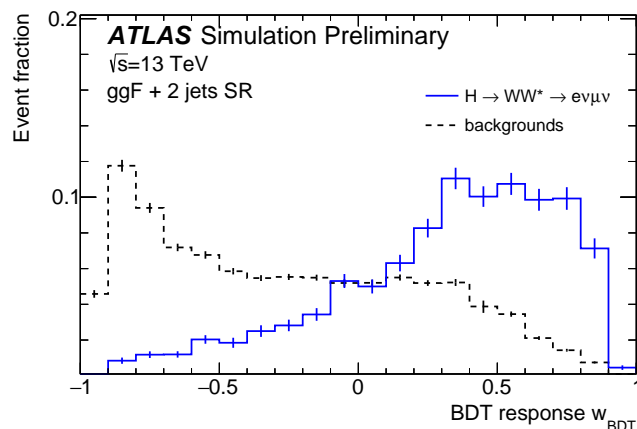
ggF+ 2 jets analysis

Figure 10: Shape comparison of the BDT response w_{BDT} distribution between $H(\to WW^* \to e\nu\mu\nu)$ + 2 jets events and the sum of backgrounds. The distribution for H + 2 jets represents the sum of events produced via the ggF +2 jets and VBF production modes. Both distributions are normalised to unit area.
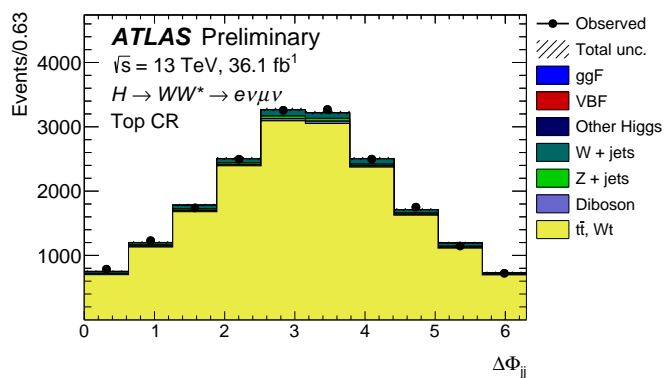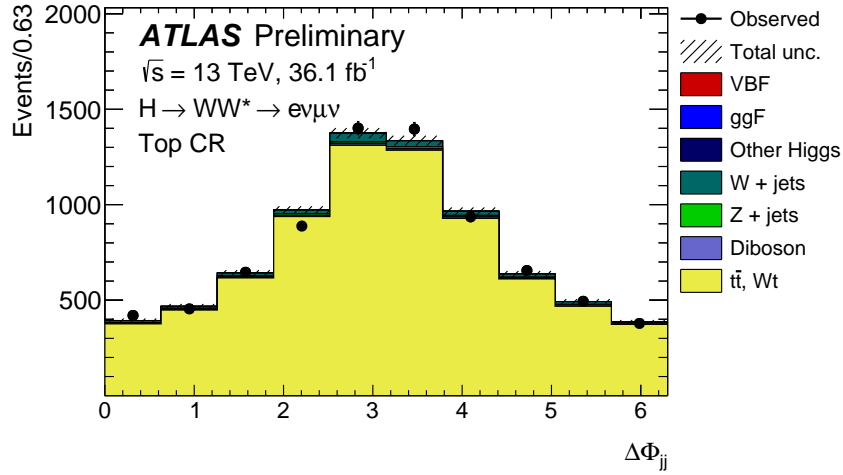

Figure 11: The $\Delta\Phi_{jj}$ distribution in the top control region of the ggF +2 jets analysis, with signal and background yields fixed from the fit to $\tan\alpha$ using shape and rate information. The shaded areas depict the total uncertainty.
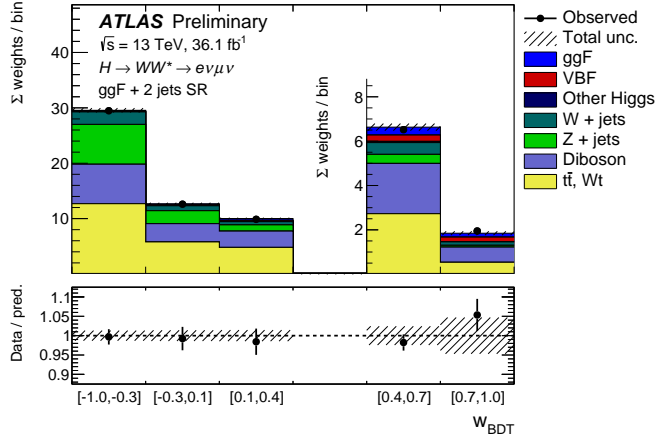
Figure 12: Weighted w_{BDT} post-fit distribution in the ggF +2 jets signal region, with signal and background yields fixed from the fit to $\mu^{ggF+2jets}$. Data-to-simulation ratios are shown at the bottom of the plot. The shaded areas depict the total uncertainty.
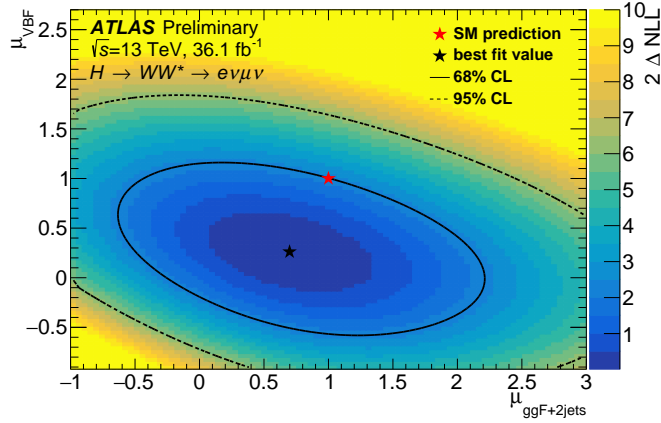
Figure 13: 68% and 95% CL two-dimensional likelihood contours of the coupling strength parameters $\mu^{ggF+2jets}$ and μ^{VBF} for a fit to the ATLAS data within the ggF + 2 jets SR. The best fit value is represented as a black star, while the SM prediction is represented by a red star. The signal strength parameters of the ggF + 2 jets and VBF processes are constrained to be $\mu^{ggF+2jets} = 0.7 \pm 0.4(\text{stat.})^{+0.8}_{-0.7}(\text{syst.})$ and $\mu^{VBF} = 0.4 \pm 0.4(\text{stat.})^{+0.4}_{-0.3}(\text{syst.})$, respectively and show a moderate negative correlation as their linear correlation coefficient is found to be -0.34.

VBF analysis

Figure 14: The $\Delta\Phi_{jj}$ distribution in the top control region of the VBF analysis, with signal and background yields fixed from the fit to a_L using shape and rate information. The shaded areas depict the total uncertainty.
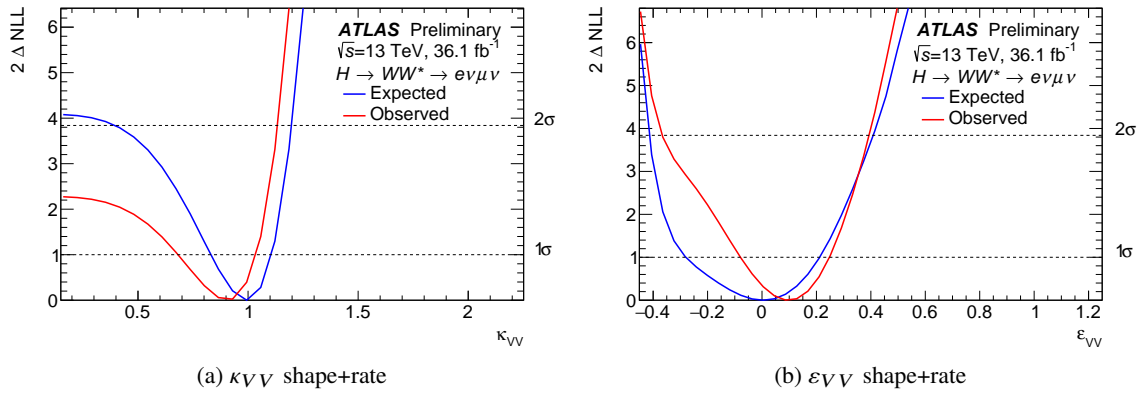

(a) κ_{VV} shape+rate

(b) ε_{VV} shape+rate

Figure 15: Likelihood scans over κ_{VV} (a) and ε_{VV} (b). The fits are performed using both shape + rate information. All relevant experimental and theoretical systematics are considered in the fit.
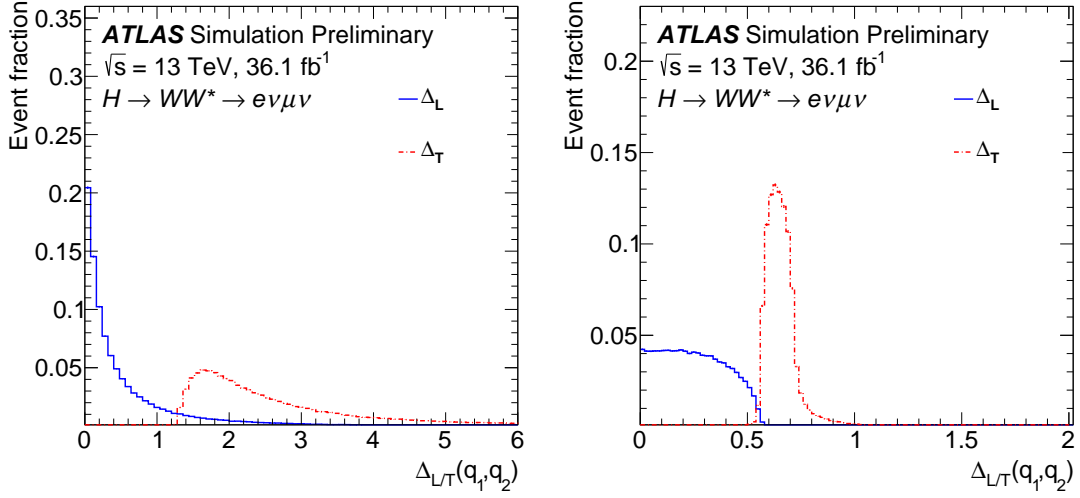
Figure 16: Generator-level comparison of the distributions to the functions $\Delta_L(q_1, q2)$ and $\Delta_T(q_1, q2)$ for the incoming (left) and outgoing (right) bosons' momenta q_1 and q_2.

References

[1]   ATLAS Collaboration, *Observation of a new particle in the search for the Standard Model Higgs boson with the ATLAS detector at the LHC*, Phys. Lett. **B716** (2012) 1, arXiv: `1207.7214 [hep-ex]` (cit. on p. 2).

[2]   CMS Collaboration, *Observation of a new boson at a mass of 125 GeV with the CMS experiment at the LHC*, Phys. Lett. **B716** (2012) 30, arXiv: `1207.7235 [hep-ex]` (cit. on p. 2).

[3]   ATLAS and CMS Collaborations, *Combined Measurement of the Higgs Boson Mass in pp Collisions at $\sqrt{s}$ = 7 and 8 TeV with the ATLAS and CMS Experiments*, Phys. Rev. Lett. **114** (2015) 191803, arXiv: `1503.07589 [hep-ex]` (cit. on p. 2).

[4]   ATLAS Collaboration, *Evidence for the spin-0 nature of the Higgs boson using ATLAS data*, Phys. Lett. **B726** (2013) 120, arXiv: `1307.1432 [hep-ex]` (cit. on p. 2).

[5]   ATLAS Collaboration, *Study of the spin and parity of the Higgs boson in diboson decays with the ATLAS detector*, Eur. Phys. J. **C75** (2015) 476, [Erratum: Eur. Phys. J. **C76** (2016) 152], arXiv: `1506.05669 [hep-ex]` (cit. on p. 2).

[6]   CMS Collaboration, *Study of the Mass and Spin-Parity of the Higgs Boson Candidate Via Its Decays to Z Boson Pairs*, Phys. Rev. Lett. **110** (2013) 081803, arXiv: `1212.6639 [hep-ex]` (cit. on p. 2).

[7]   ATLAS Collaboration, *Test of CP invariance in vector-boson fusion production of the Higgs boson in the $H \to \tau\tau$ channel in proton−proton collisions at $\sqrt{s}$ = 13 TeV with the ATLAS detector*, Phys. Lett. B **805** (2020) 135426, arXiv: `2002.05315 [hep-ex]` (cit. on p. 2).

[8]   CMS Collaboration, *Constraints on anomalous HVV couplings from the production of Higgs bosons decaying to τ lepton pairs*, Phys. Rev. D **100** (2019) 112002, arXiv: `1903.06973 [hep-ex]` (cit. on p. 2).

[9] CMS Collaboration, *Combined search for anomalous pseudoscalar HVV couplings in VH(H → bb̄) production and H → VV decay*, Phys. Lett. **B759** (2016) 672, arXiv: 1602.04305 [hep-ex] (cit. on p. 2).

[10] ATLAS Collaboration, *CP Properties of Higgs Boson Interactions with Top Quarks in the tt̄H and tH Processes Using H → γγ with the ATLAS Detector*, Phys. Rev. Lett. **125** (6 2020) 061802 (cit. on p. 2).

[11] CMS Collaboration, *Measurements of tt̄H Production and the CP Structure of the Yukawa Interaction between the Higgs Boson and Top Quark in the Diphoton Decay Channel*, Phys. Rev. Lett. **125** (2020) 061801, arXiv: 2003.10866 [hep-ex] (cit. on p. 2).

[12] M. Dolan et al., *Constraining CP-violating Higgs Sectors at the LHC using gluon fusion*, Phys. Rev. **D90** (2014) 073008, arXiv: 1406.3322 [hep-ph] (cit. on p. 2).

[13] CMS Collaboration, *Measurements of properties of the Higgs boson decaying to a W boson pair in pp collisions at √s = 13 TeV*, Phys. Lett. B **791** (2019) 96, arXiv: 1806.05246 [hep-ex] (cit. on p. 2).

[14] CMS Collaboration, *Constraints on anomalous HVV couplings from the production of Higgs bosons decaying to τ lepton pairs*, Phys. Rev. D **100** (2019) 112002, arXiv: 1903.06973 [hep-ex] (cit. on p. 2).

[15] CMS Collaboration, *Measurements of the Higgs boson width and anomalous HVV couplings from on-shell and off-shell production in the four-lepton final state*, Phys. Rev. D **99** (2019) 112003, arXiv: 1901.00174 [hep-ex] (cit. on p. 2).

[16] ATLAS Collaboration, *Search for Higgs bosons produced via vector-boson fusion and decaying into bottom quark pairs in √s = 13 TeV pp collisions with the ATLAS detector*, Phys. Rev. D **98** (2018) 052003, arXiv: 1807.08639 [hep-ex] (cit. on p. 2).

[17] ATLAS Collaboration, *Measurements of gluon-gluon fusion and vector-boson fusion Higgs boson production cross-sections in the H → WW* → eνμν decay channel in pp collisions at √s = 13 TeV with the ATLAS detector*, Phys. Lett. **B789** (2019) 508, arXiv: 1808.09054 [hep-ex] (cit. on pp. 2, 10–13, 18).

[18] D. B. Kaplan et al., *SU(2) × U(1) breaking by vacuum misalignment*, Phys. Lett. **136B** (1984) 183 (cit. on p. 2).

[19] D. B. Kaplan et al., *Composite Higgs scalars*, Phys. Lett. **136B** (1984) 187 (cit. on p. 2).

[20] P. Artoisenet et al., *A framework for Higgs characterisation*, JHEP **11** (2013) 043, arXiv: 1306.6464 [hep-ph] (cit. on p. 3).

[21] S. Frixione et al., *Matching NLO QCD computations and parton shower simulations*, JHEP **0206** (2002) 029, arXiv: hep-ph/0204244 [hep-ph] (cit. on p. 3).

[22] F. Maltoni et al., *Higgs characterisation at NLO in QCD: CP properties of the top-quark Yukawa interaction*, Eur. Phys. J. **C74** (2014) 3065, arXiv: 1407.5089 [hep-ph] (cit. on pp. 3, 6).

[23] J. Brehmer et al., *Polarized WW scattering on the Higgs pole*, Phys.Rev. **D90** (2014) 054023, arXiv: 1404.5951 [hep-ph] (cit. on pp. 4, 6, 19).

[24] A. Greljo et al., *Electroweak Higgs production with HIGGSPO at NLO QCD*, Eur. Phys. J. **C77** (2017) 838, arXiv: 1710.04143 [hep-ph] (cit. on p. 4).

[25] M. Gonzalez-Alonso et al., *Pseudo-observables in Higgs decays*, Eur. Phys. J. C **75** (2015) 128, arXiv: 1412.6038 [hep-ph] (cit. on p. 4).

[26] ATLAS Collaboration, *The ATLAS Experiment at the CERN Large Hadron Collider*, JINST **3** (2008) S08003 (cit. on p. 5).

[27] ATLAS Collaboration, *ATLAS data quality operations and performance for 2015–2018 data-taking*, JINST **15** (2020) P04003, arXiv: `1911.04632 [physics.ins-det]` (cit. on p. 6).

[28] ATLAS Collaboration, *Improved luminosity determination in pp collisions at $\sqrt{s} = 7$ TeV using the ATLAS detector at the LHC*, Eur. Phys. J. **C73** (2013) 2518, arXiv: `1302.4393 [hep-ex]` (cit. on p. 6).

[29] J. Alwall et al., *The automated computation of tree-level and next-to-leading order differential cross sections, and their matching to parton shower simulations*, JHEP **07** (2014) 079, arXiv: `1405.0301 [hep-ph]` (cit. on p. 6).

[30] R. Ball et al., *Parton distributions for the LHC run II*, JHEP **04** (2015) 040, arXiv: `1410.8849 [hep-ph]` (cit. on p. 6).

[31] T. Sjöstrand et al., *A Brief Introduction to PYTHIA 8.1*, Comput. Phys. Commun. **178** (2008) 852, arXiv: `0710.3820 [hep-ph]` (cit. on pp. 6, 7).

[32] ATLAS Collaboration, *ATLAS Pythia 8 tunes to 7 TeV data*, tech. rep. ATL-PHYS-PUB-2014-021, CERN, 2014, URL: `https://cds.cern.ch/record/1966419` (cit. on p. 6).

[33] F. Demartin et al., 'Higgs characterisation: NLO and parton-shower effects', *2nd Toyama International Workshop on Higgs as a Probe of New Physics*, 2015, arXiv: `1505.07081 [hep-ph]` (cit. on p. 6).

[34] S. Alioli et al., *A general framework for implementing NLO calculations in shower Monte Carlo programs: the POWHEG BOX*, JHEP **06** (2010) 043, arXiv: `1002.2581 [hep-ph]` (cit. on p. 6).

[35] ATLAS & CMS Collaborations, *Combined Measurement of the Higgs Boson Mass in pp Collisions at $\sqrt{s} = 7$ and 8 TeV with the ATLAS and CMS Experiments*, Phys. Rev. Lett. **114** (2015) 191803, arXiv: `1503.07589 [hep-ex]` (cit. on p. 6).

[36] A. Djouadi et al., *HDECAY: A program for Higgs boson decays in the Standard Model and its supersymmetric extension*, Comput. Phys. Commun. **108** (1998) 56, arXiv: `hep-ph/9704448` (cit. on p. 6).

[37] LHC Higgs Cross Section Working Group, *Handbook of LHC Higgs Cross Sections: 4. Deciphering the Nature of the Higgs Sector*, (2016), arXiv: `1610.07922 [hep-ph]` (cit. on pp. 6, 13).

[38] M. Cacciari et al., *Fully Differential Vector-Boson-Fusion Higgs Production at Next-to-Next-to-Leading Order*, Phys. Rev. Lett. **115** (2015) 082002, [Erratum: Phys. Rev. Lett. 120 (2018) 139901], arXiv: `1506.02660 [hep-ph]` (cit. on p. 6).

[39] A. Denner et al., *HAWK 2.0: A Monte Carlo program for Higgs production in vector-boson fusion and Higgs strahlung at hadron colliders*, Comput. Phys. Commun. **195** (2015) 161, arXiv: `1412.5390 [hep-ph]` (cit. on p. 6).

[40] J. M. Lindert et al., *An NLO+PS generator for $t\bar{t}$ and Wt production and decay including non-resonant and interference effects*, Eur. Phys. J. **C76** (2016) 691, arXiv: `1607.04538 [hep-ph]` (cit. on p. 6).

[41] M. Czakon et al., *Top++: A program for the calculation of the top-tair cross-section at hadron colliders*, Comput.Phys.Commun. **185** (2011) 2930, arXiv: `1112.5675 [hep-ph]` (cit. on p. 7).

[42] P. Z. Skands et al., *Tuning Monte Carlo generators: The Perugia tunes*, Phys. Rev. **D82** (2010) 074018, arXiv: `1005.3457 [hep-ph]` (cit. on p. 7).

[43] H. L. Lai et al., *New parton distributions for collider physics*, Phys. Rev. **D82** (2010) 074024, arXiv: 1007.2241 [hep-ph] (cit. on p. 7).

[44] S. Frixione et al., *Single-top hadroproduction in association with a W boson*, JHEP **07** (2008) 029, arXiv: 0805.3067 [hep-ph] (cit. on p. 7).

[45] ATLAS Collaboration, *Multi-Boson Simulation for 13 TeV ATLAS Analyses*, tech. rep. ATL-PHYS-PUB-2017-005, CERN, 2017, URL: https://cds.cern.ch/record/2261933 (cit. on pp. 7, 12).

[46] S. Hoeche et al., *QCD matrix elements + parton showers. The NLO case*, JHEP **04** (2013) 027, arXiv: 1207.5030 [hep-ph] (cit. on p. 7).

[47] F. Cascioli et al., *Scattering Amplitudes with Open Loops*, Phys. Rev. Lett. **108** (2012) 111601, arXiv: 1111.5206 [hep-ph] (cit. on p. 7).

[48] ATLAS Collaboration, *The ATLAS Simulation Infrastructure*, Eur. Phys. J. **C70** (2010) 823, arXiv: 1005.4568 [physics.ins-det] (cit. on p. 7).

[49] GEANT4 Collaboration, *GEANT4– a simulation toolkit*, Nucl. Instrum. Meth. **A506** (2003) 250 (cit. on p. 7).

[50] ATLAS Collaboration, *Performance of the ATLAS trigger system in 2015*, Eur. Phys. J. **C77** (2017) 317, arXiv: 1611.09661 [hep-ex] (cit. on p. 7).

[51] ATLAS Collaboration, *Electron reconstruction and identification in the ATLAS experiment using the 2015 and 2016 LHC proton-proton collision data at $\sqrt{s}$ = 13 TeV*, Eur. Phys. J. **C79** (2019) 639, arXiv: 1902.04655 [physics.ins-det] (cit. on pp. 8, 12).

[52] ATLAS Collaboration, *Muon reconstruction performance of the ATLAS detector in proton-proton collision data at $\sqrt{s}$ =13 TeV*, Eur. Phys. J. **C76** (2016) 292, arXiv: 1603.05598 [hep-ex] (cit. on pp. 8, 12).

[53] G. S. Salam et al., *The anti-k_t jet clustering algorithm*, JHEP **0804** (2008) 063, arXiv: 0802.1189 [hep-ph] (cit. on p. 8).

[54] ATLAS Collaboration, *Jet energy scale measurements and their systematic uncertainties in proton-proton collisions at $\sqrt{s}$ = 13 TeV with the ATLAS detector*, Phys. Rev. D **96** (2017) 072002, arXiv: 1703.09665 [hep-ex] (cit. on p. 8).

[55] ATLAS Collaboration, *Tagging and suppression of pileup jets*, (2014), URL: https://cds.cern.ch/record/1700870 (cit. on p. 9).

[56] ATLAS Collaboration, *Performance of b-Jet Identification in the ATLAS Experiment*, (2015), arXiv: 1512.01094 [hep-ex] (cit. on p. 9).

[57] ATLAS Collaboration, *Optimisation of the ATLAS b-tagging performance for the 2016 LHC Run*, tech. rep. ATL-PHYS-PUB-2016-012, CERN, 2016, URL: https://cds.cern.ch/record/2160731 (cit. on p. 9).

[58] ATLAS Collaboration, *Performance of missing transverse momentum reconstruction for the ATLAS detector in the first proton-proton collisions at at $\sqrt{s}$= 13 TeV*, tech. rep. ATL-PHYS-PUB-2015-027, CERN, 2015, URL: https://cds.cern.ch/record/2037904 (cit. on p. 9).

[59] ATLAS Collaboration, *Expected performance of missing transverse momentum reconstruction for the ATLAS detector at $\sqrt{s}$ = 13 TeV*, tech. rep. ATL-PHYS-PUB-2015-023, CERN, 2015, URL: https://cds.cern.ch/record/2037700 (cit. on p. 9).

[60] T. Plehn et al., *A Method for identifying $H \rightarrow \tau^+\tau^- \rightarrow e^\pm \mu^\mp p_T$ at the CERN LHC*, Phys. Rev. **D61** (2000) 093005, arXiv: hep-ph/9911385 [hep-ph] (cit. on p. 9).

[61] ATLAS Collaboration, *Measurements of b-jet tagging efficiency with the ATLAS detector using $t\bar{t}$ events at $\sqrt{s}$ = 13 TeV*, JHEP **08** (2018) 089, arXiv: 1805.01845 [hep-ex] (cit. on p. 12).

[62] ATLAS Collaboration, *Jet Calibration and Systematic Uncertainties for Jets Reconstructed in the ATLAS Detector at $\sqrt{s}$ = 13 TeV*, tech. rep. ATL-PHYS-PUB-2015-015, CERN, 2015, URL: https://cds.cern.ch/record/2037613 (cit. on p. 12).

[63] ATLAS Collaboration, *Electron and photon energy calibration with the ATLAS detector using 2015–2016 LHC proton-proton collision data*, JINST **14** (2019) P03017, arXiv: 1812.03848 [hep-ex] (cit. on p. 12).

[64] ATLAS Collaboration, *E_T^{miss} performance in the ATLAS detector using 2015-2016 LHC p-p collisions*, tech. rep. ATLAS-CONF-2018-023, CERN, 2018, URL: http://cds.cern.ch/record/2625233 (cit. on p. 12).

[65] ATLAS Collaboration, *Luminosity determination in pp collisions at $\sqrt{s}$ = 8 TeV using the ATLAS detector at the LHC*, Eur. Phys. J. **C76** (2016) 653, arXiv: 1608.03953 [hep-ex] (cit. on p. 12).

[66] ATLAS Collaboration, *A morphing technique for signal modelling in a multidimensional space of coupling parameters*, tech. rep. ATL-PHYS-PUB-2015-047, CERN, 2015, URL: https://cds.cern.ch/record/2066980 (cit. on p. 14).

[67] M. Baak et al., *Interpolation between multi-dimentional histograms using a new non-linear moment morphing method*, (2014), arXiv: 1410.7388 [hep-ex] (cit. on p. 14).